

Fear the Shadows of the Giants: On Secular Perturbations in Circumstellar Habitable Zones of
Double Stars

ÁKOS BAZSÓ¹ AND ELKE PILAT-LOHINGER¹

¹*Department of Astrophysics*

University of Vienna

Türkenschanzstrasse 17

A-1180 Vienna, Austria

(Received XXX, 2019; Revised YYY, 2020; Accepted ZZZ, 2020)

Submitted to AJ

ABSTRACT

After the detection of extrasolar planets in binary and multiple star systems questions arose about their dynamics and habitability. In this study we investigate a five-dimensional parameter space for wide binary stars with a massive planet beyond the habitable zone (HZ). Our aim is to reveal those orbital and physical parameter combinations that expose bodies in the primary star's HZ to secular perturbations. Building upon an established semi-analytical model, we combine two separate analytical models into a new one to treat the restricted four-body problem. We apply this new Combined Analytical Model (CAM) to different synthetic systems and systematically map the occurrence of secular resonances (SR). These maps are then visualized as two-dimensional sections of the parameter space. The CAM model has a median error below 3 % relative

to numerical reference simulations. We also derive a simplified CAM that performs well for hierarchical systems with moderate to large separations between the bodies. Our results show that SR appear in the HZ even for large secondary star distances (up to > 1000 au) if either (i) the planet’s distance is larger than Jupiter’s, or (ii) its mass is about Saturn’s or lower. Changes in the secondary star’s eccentricity by stellar flybys or galactic tides can push a formerly dynamically quiet HZ to a high-eccentricity state. Based on these results we provide the easy-to-use online tool ‘SHaDoS’ that evaluates the CAM for a given user input and traces the locations of SR in the HZ in two-dimensional parameter space plots.

Keywords: binaries: general; celestial mechanics: restricted four-body problem; habitability; methods: analytical; planets and satellites: dynamical evolution and stability; planets and satellites: terrestrial planets

1. INTRODUCTION

Observational surveys revealed that a considerable fraction of stars in the solar neighbourhood are members of binary and multiple star systems. In this context, [Duquennoy et al. \(1991\)](#) and [Raghavan et al. \(2010\)](#) established that in the solar neighbourhood up to distances of $d \leq 25$ pc about 40 – 45 % of all Sun-like stars with spectral types F6–K3 are members of binary and multiple star systems, independent of whether or not they are hosting extrasolar planets (or short exoplanets). [Tokovinin \(2014\)](#) found for a sample of about 4800 F- and G-type main-sequence stars within 67 pc of the Sun that 33 % of the targets belong to binary star systems. Further details on the frequency and main characteristics of multiple star systems can be found in the review of [Duchêne and Kraus \(2013\)](#).

The detection of exoplanets also in binary and multi-stellar systems showed that planetary companions are not restricted to single stars. However, it is uncertain how favourable stellar multiplicity really is for the presence of exoplanets. Based on the discovered exoplanet population [Raghavan et al. \(2006\)](#), [Desidera and Barbieri \(2007\)](#), [Mugrauer and Neuhäuser \(2009\)](#), and [Roell et al. \(2012\)](#)

estimated the stellar multiplicity. These studies yield that about 10–15 % of the detected exoplanets reside in binaries, while only ~ 2 % of all known exoplanet host stars are members of multiple star systems with three or more components. The *Catalogue of Exoplanets in Binary and Multiple Star Systems*¹ of Schwarz et al. (2016) provides an up-to-date compilation of all binary and multiple star systems hosting exoplanets.

Although many exoplanets have been found in both binary and multiple star systems, it is unclear whether or not these environments are more hostile than single star systems for the presence of planets. There are different views on the efficiency of planet formation in binary stars and the impact of the stellar companion’s perturbations. On the one hand, simulations of protoplanetary disks were able to form both terrestrial and giant planets even in tight binary systems, see e.g. Boss (2006); Quintana et al. (2007); Rafikov (2013); Bromley and Kenyon (2015); Jang-Condell (2015). These studies relate to rather tight systems with stellar separations of < 100 astronomical units (au), such as the poster cases γ Cephei and HD 41004 with ~ 20 au. On the other hand there are indications that the occurrence rate of circumstellar planets is strongly influenced by close binary companions (see Kley and Nelson 2010; Müller and Kley 2012; Wang et al. 2014; Kraus et al. 2016). For more comprehensive reviews on planet formation in binary star systems refer to Zhou et al. (2012), Thebault and Haghighipour (2015), and Pilat-Lohinger et al. (2019).

Apart from the circumstances of planet formation in binaries also the long-term stability of planetary systems is an issue. In this study we focus exclusively on circumstellar (S-type) planetary systems of binary stars (Dvorak 1982). Different kinds of resonances play a key role for the orbital evolution of the planets, e.g. mean motion and secular resonances.

Mean motion resonances (MMR) involve combinations of orbital frequencies and their overlap has already been identified to be crucial in triggering chaos (Mudryk and Wu 2006; Hadden and Lithwick 2018). The occurrence of circumstellar planets depends sensitively on the interactions with the outer stellar companion and on its orbital parameters (Rabl and Dvorak 1988; Holman and Wiegert 1999;

¹ <https://www.univie.ac.at/adg/schwarz/multiple.html>

Pilat-Lohinger and Dvorak 2002). All these studies have focused on the stability of prograde planets though, but retrograde resonances offer a stabilizing mechanism beyond the established stability borders for the prograde case. Morais and Giuppone (2012) and Morais and Namouni (2013) studied retrograde resonances for binary stars in the context of the circular spatial restricted three-body problem. These works were based on the study of Gayon and Bois (2008) who demonstrated that retrograde MMR can stabilize compact multi-planetary systems. In the former studies of binary systems the (retrograde) resonant terms were identified in the expansion of the disturbing function and two main aspects of the stabilizing mechanism were discussed: first, the eccentricity forcing for a prograde planet is larger than for a retrograde one (i.e. different exponents for the eccentricity in the leading term of the expansion), and second the overlap among nearby resonances occurs at larger perturber masses for retrograde planets.

Secular interactions are related to apsidal and nodal precession frequencies and constitute another way how the stellar companion can influence circumstellar planetary systems. Similar to MMR, SR affect not only prograde but retrograde orbits as well, and can even induce a switch between these two types of orbital motion. Naoz et al. (2013) investigated the secular dynamics of hierarchical three-body systems and derived an octupole order secular approximation to the equations of motion. From their model they found a qualitatively different dynamical evolution for an inner body that can become highly eccentric and would then oscillate between prograde and retrograde motion when it is perturbed by an eccentric outer body. Li and Christou (2017) applied a semi-analytical model to investigate SR for prograde and retrograde orbits in a restricted four-body problem. They identified the critical angles of the strongest SR that are formed by linear combinations of apsidal and nodal differences of the two adjacent orbits. In general, even initially circular and coplanar planetary orbits can be strongly altered by secular perturbations from a massive, eccentric and inclined outer companion. Takeda et al. (2008) investigated the angular momentum transfer from a stellar companion to weakly or rigidly coupled planetary systems. They identified that this cascaded angular momentum transfer through the system leads to a significant eccentricity excitation for the innermost planet for a certain range of outer planet parameters. In a similar study, Pu and Lai (2018)

found that eccentricities and mutual inclinations of weakly coupled multi-planet systems are more effectively excited by external companions than for their strongly coupled counterparts (i.e. compact planetary systems).

Still another type of resonant forcing exerted by the binary companion involves the evection resonance (Frouard et al. 2010; Touma and Sridhar 2015) that combines the orbital precession frequency of an inner planetary orbit with the orbital motion of the outer secondary star (or another perturber). This process can lead to large amplitude oscillations of the planetary eccentricities and mutual inclinations, or even to the disruption of the planetary system. Recently, Marzari and Gallina (2016) demonstrated that the outer stability border of planetary orbits in multi-planet systems of binaries is destabilized by overlap of MMR and SR (both linear and non-linear ones).

In spite of all these different mechanisms to disrupt planetary systems it is not hopeless to find terrestrial planets in binaries, preferably even in the habitable zone (HZ). Funk et al. (2015) examined four different tight binary systems with a known massive planet to explore their potential of being able to host additional habitable terrestrial planets. They concluded that two systems are promising candidates and permit dynamically stable orbits in the HZ. However, the identification of suitable systems requires a thorough knowledge of the locations of resonances. In case of MMR this is trivial, but it is more difficult to find the locations of SR. To tackle this task, Pilat-Lohinger et al. (2016) and Bazzó et al. (2017) described a semi-analytical method that simplifies matters. That method determines the orbital precession frequencies for the perturbers and allows to estimate the positions of linear SR for test particles. However, the method is valid for the system as it is, i.e. for the instantaneous orbital parameters of the perturbers; if the parameters change with time or by improved observations, then the analysis would need to be repeated.

In this work we aim at a more global description of the dynamics in a binary star system with a giant planet. Our goal is to reveal parameter combinations that expose bodies (terrestrial planets) in the primary star's HZ to secular perturbations. These parameters cover all relevant observables, in particular masses, orbital distances, and eccentricities, such that observational uncertainties are implicitly included into the analysis. We investigate this multi-dimensional parameter space by means

of a combination of analytical models. This allows to quickly identify the locations of SR and to indicate whether to safely exclude systems with a-priori perturbed HZs or to perform a subsequent detailed stability analysis with complementary tools. A possible application of the method is for newly discovered exoplanetary systems of binary stars, where it would help to exclude those systems that cannot host planets in the HZ in low eccentricity orbits. This, in turn, renders the method especially valuable as a guide to select such binary star systems for in-depth observations that would allow planets in the HZ from a dynamical point of view.

The outline of the paper is as follows. We describe the basic dynamical model along with the analytical methods employed for the parameter search in section 2. Subsequently, in section 3, we first investigate the performance of the analytical models relative to reference data from numerical simulations, and then present the results on the SR location depending on the system parameters. Section 4 contains a discussion of the results and how they compare to other studies. Finally, section 5 highlights the main results. Additionally, in Appendix A we introduce an online tool that is based on the models from section 2 and can be used to create plots similar to those in this article.

2. THEORY AND MODELS

Our main goal is to identify those combinations of physical and orbital parameters for binary star systems with a circumstellar giant planet that lead to secular perturbations inside the host star’s habitable zone. First, we provide the HZ model and state the HZ location and its extent in section 2.1. Next, we introduce the dynamical model for the secular evolution of the system in section 2.2, and define the main relation for the secular frequencies. On the basis of this relation we show how to use the combined analytical model (CAM) that consists of two consecutive steps, each of them given by a simple analytical expression, that are described in sections 2.2.1 and 2.2.2. Finally, we demonstrate some of the properties of the CAM and derive a simplified form for it. Table 1 contains a list of the variable names used in this work, together with a short description for a quick overview.

2.1. *Habitable zone*

Table 1. Glossary of important variables used in this work.

Variable	Description
a_B	semi-major axis of secondary star (component B)
a_{GP}	semi-major axis of giant planet
a_{IHZ}	inner border of host star's habitable zone
a_{OHZ}	outer border of host star's habitable zone
a_{TP}	semi-major axis of test planet
α	semi-major axis ratio, e.g. a_{GP}/a_B
$b_{3/2}^{(1)}$	Laplace coefficient
γ	mass ratio, e.g. m_B/m_A
δ_g	empirical correction term for the secular frequency g , see eq. (4)
e_B	eccentricity of secondary star (component B)
e_{GP}	eccentricity of giant planet
g_{GP}	secular frequency of giant planet
g_{TP}	secular frequency of test planet
m_A	mass of primary star (component A)
m_B	mass of secondary star (component B)
m_{GP}	mass of giant planet
m_{TP}	mass of test planet, equals zero by definition
n_{GP}	mean motion of giant planet
n_{TP}	mean motion of test planet

There exist various models for calculating HZs for binary stars and in particular circumstellar HZs, e.g. [Eggl et al. \(2012\)](#), [Kaltenegger and Haghighipour \(2013\)](#), [Cuntz \(2014\)](#), and its update in [Wang and Cuntz \(2019\)](#). A common point of all these models is that they extend the classical concept of habitable zones of single stars, see e.g. [Kasting et al. \(1993\)](#) or [Kopparapu et al. \(2014\)](#), by taking into account multiple sources of radiation, and to some extent also the dynamical evolution of objects.

In case of circumstellar planets, the HZ location still primarily depends on the luminosity (mass) and effective temperature of the host star. Thus, from a practical point of view, it is permissible to approximate the binary star HZ as that of a single star HZ (SSHZ), because in the following we will typically deal with rather large stellar separations (on the order of some hundred au). In such cases the secondary’s contribution is practically negligible; for stellar separations > 20 au the binary star HZ borders typically shift by < 0.1 au relative to the SSHZ.

For our purposes we fix the host star’s spectral type² to G2 V, which gives a solar analogue star with mass $1 M_{\odot}$, luminosity $1 L_{\odot}$, and effective temperature 5780 K. With this set of parameters we obtain a HZ that ranges from the inner HZ border (IHZ), $a_{\text{IHZ}} = 0.95$ au, to the outer HZ border (OHZ), $a_{\text{OHZ}} = 1.68$ au, according to the model of [Kopparapu et al. \(2014\)](#).

2.2. Dynamical model

Let us assume a binary star system that consists of two stellar components and a (Jupiter-like) giant planet (GP), with the restrictions that all bodies are in coplanar and prograde motion. We will denote the planet hosting star (component A) the primary star, while the distant perturber (component B) will be named the secondary star. The planet is in circumstellar motion (S-type; [Dvorak 1982](#)) about the host star, and we further assume that it is located exterior to the habitable zone. [Figure 1](#) shows a sketch of this situation. In the figure, the horizontal errorbars indicate the range of distances from pericenter to apocenter that each object can cover due to its eccentricity. The secondary star must maintain a minimum distance from the primary, in order for the giant planet to remain inside the host star’s stability region for all times (see [Rabl and Dvorak 1988](#), [Holman and Wiegert 1999](#), and [Pilat-Lohinger and Dvorak 2002](#) for details).

A binary star with a circumstellar giant planet forms a hierarchical system. In terms of dynamical perturbations, the distant secondary star perturbs the giant planet, which itself would pass the perturbations on to any bodies in the HZ. By virtue of the vastly different masses of the bodies

² Without loss of generality; this choice only affects the HZ limits that can be easily calculated for other spectral types (masses).

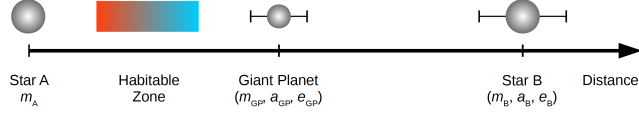


Figure 1. Sketch of the dynamical configuration of a coplanar binary star system. A giant planet (GP) orbits the primary star (star A, or host star) exterior to its habitable zone in circumstellar motion. The more distant secondary star (star B) acts as a perturber to the whole system. Horizontal error bars indicate the radial excursions due to the object’s eccentricity. Object sizes and distances are not to scale.

entangled in this interaction, an initially small perturbation from the secondary star can result in huge perturbations in the HZ. The focus is on secular interactions, where orbital precession frequencies play a major role over extended periods of time, as opposed to short period effects by orbital resonances.

Foremost, the strongest secular perturbations arise at locations where the linear combinations of a test planet’s orbital precession frequency, g_{TP} , and that of the giant planet, g_{GP} , form small numbers

$$q g_{TP} - p g_{GP} \approx 0, \quad (1)$$

i.e. when the two frequencies are close to form an integer combination $g_{TP}/g_{GP} \approx p/q$ (with $p, q \in \mathbb{Z}$). This relation forms the basis for all subsequent investigations. Similar to MMR, the strongest effects arise when $p = q = 1$, which gives rise to a linear SR. The general case with $p \neq q$ ($p > 0, q > 0$) is called a non-linear secular resonance (see [Knezevic et al. 1991](#), for the definitions of linear and non-linear SR). Any given SR’s strength depends on the specific frequency combination (p, q) . In case of apsidal frequencies it depends on different powers of the eccentricities, according to [Murray and Dermott \(1999, Appendix B\)](#) the leading term is $\propto e_{TP}^q e_{GP}^p$. So we can appreciate that for fixed (e_{TP}, e_{GP}) the SR with $p = q = 1$ will always be dominating, but the $p = 2, q = 1$ and $p = 1, q = 2$ resonances might show very different effects when $e_{TP} \neq e_{GP}$.

In case of an exact resonance we can recast eq. (1) into the form $q g_{TP} = p g_{GP}$. The right-hand side of this equation constitutes a three-body problem including the two stars and a giant planet; if the latter is taken to be massless, the dynamical model reduces to a restricted three-body problem. Conversely, the left-hand side inevitably forms a restricted four-body problem, which follows from

our convention to set test planet masses $m_{TP} = 0$. This duality makes it difficult to treat eq. (1) using a single formula or secular model. An unified formula would need to be applicable to both the three- and four-body problem and to be valid for a large range of parameters with high accuracy.

In fact, up to now our method of choice was the semi-analytical model (SAM) described in [Pilat-Lohinger et al. \(2016\)](#) and [Bazsó et al. \(2017\)](#). The SAM starts from the basic equation above and determines the exact location for which $q g_{TP} - p g_{GP} = 0$ is fulfilled in terms of a_{TP} . It treats the global restricted four-body problem binary-star – giant planet – test planet as two coupled three-body problems. In a first step, the giant planet’s precession frequency g_{GP} in eq. (1) is determined numerically by frequency analysis from a numerical simulation of the binary-star – giant planet subsystem. Then the calculation of g_{TP} is performed for fixed parameters of the secondary star and giant planet with the determined (and constant) value of g_{GP} by means of any suitable analytical formula.

The trade-off with an approach like the SAM is that it is less flexible when it comes to scan through a multi-dimensional parameter space. However, a combination of analytical models for both frequencies in eq. (1) would facilitate such studies and allow to investigate a large variety of binary star configurations. In [Bazsó and Pilat-Lohinger \(2017\)](#) we have investigated a number of analytical secular models for the giant planet precession frequency, g_{GP} . It turned out that two models are promising candidates for this task, namely the models of [Andrade-Ines and Eggl \(2017\)](#) and [Georgakarakos \(2003, 2009\)](#). The latter one provides a framework for the eccentricity evolution (on short and secular time-scales) in the hierarchical full three-body problem, while the former one is only valid for the restricted problem. In the following, we describe the transition from the SAM to the new Combined Analytical Model (CAM) that involves a combination of two different analytical models that are connected in order to solve eq. (1).

2.2.1. Analytical model for giant planet frequency

[Andrade-Ines and Eggl \(2017\)](#) established a simple and accurate secular model for the restricted three-body problem, i.e. the giant planet acts like a massless body relative to the two stars. Their model is also applicable in case of strongly perturbed three-body systems, i.e. when the secondary

star’s distance from the primary is just two to three times that of the giant planet. The main relation is given by

$$g_{GP} = g_H(1 - \delta_g), \quad (2)$$

where g_H is a first order approximation (in masses) to g_{GP} due to Heppenheimer’s formula (Heppenheimer 1978),

$$g_H = \frac{3}{4} n_{GP} \left(\frac{m_B}{m_A} \right) \left(\frac{a_{GP}}{a_B} \right)^3 (1 - e_B^2)^{-3/2}, \quad (3)$$

and n_{GP} is the giant planet’s mean motion. The term δ_g is an empirical correction to the frequency, and has the general form

$$\delta_g = \sum_{k=1}^M A_k \left(\frac{m_B}{m_A} \right)^{p_k} \left(\frac{a_{GP}}{a_B} \right)^{q_k} e_B^{r_k}, \quad (4)$$

with typically $M \leq 20$ coefficients A_k and various powers (p_k, q_k, r_k) ; refer to Andrade-Ines and Eggl (2017) for the actual values of these coefficients and exponents. This kind of correction to the secular precession frequency follows the spirit of previous attempts, e.g. Giuppone et al. (2011).

The model expresses the secular precession frequency g_{GP} as a polynomial function of the basic parameters mass ratio $\gamma = m_B/m_A$, semi-major axis ratio $\alpha = a_{GP}/a_B$, and perturber eccentricity e_B . Formally, Andrade-Ines and Eggl (2017) state the validity ranges of their fit as $0.1 \leq \gamma \leq 10$, $0.01 \leq \alpha \leq 0.4$, and $0 \leq e_B \leq 0.6$. This interval of mass ratios covers the full range of interest for binary star systems with a G-type primary component, from the lowest mass M-dwarves (for $\gamma = 0.1$) up to F- and A-type stars (for $\gamma \approx 2$). Larger values of γ would lead to an exceedingly fast stellar evolution of the secondary, such that it were no more a main-sequence star. The interval for the distance ratio α also covers most – if not all – currently observed exoplanets in binary systems, including cases like γ Cephei ($\alpha = 0.1$) and HD 196885 ($\alpha = 0.12$), see Bazsó et al. (2017) for a list of tight binary systems. One remaining caveat is that for some observed binary star systems the secondary’s eccentricity might be larger than $e_B = 0.6$ (e.g. for τ Bootis)³.

³ Another issue stems from the fact that the Washington Double Star catalogue lists less than 1000 systems (from a total of more than 130,000) with well-constrained stellar eccentricity. At larger stellar separations (above 100 au, i.e. in the distance range considered here) there is a deficit of observational information on the eccentricities. Therefore, there is a clear need to estimate perturbing effects on the HZ due to stellar eccentricities.

2.2.2. Analytical model for test planet frequency

According to the Laplace-Lagrange model (LLM) the secular precession frequency for a massless test planet (TP) influenced by N massive perturbers is given by

$$g_{TP} = \frac{n_{TP}}{4} \sum_{i=1}^N \left(\frac{m_i}{m_A} \right) \left(\frac{a_{TP}}{a_i} \right)^2 b_{3/2}^{(1)} \left(\frac{a_{TP}}{a_i} \right) (1 - e_i^2)^{-3/2},$$

where n_{TP} is the test planet's mean motion, and the function $b_{3/2}^{(1)}(\alpha_i)$ is a Laplace coefficient of the single scalar variable $0 \leq \alpha_i = a_{TP}/a_i < 1$ (cf. [Murray and Dermott 1999](#), chapter 6). For our dynamical model with $N = 2$ (giant planet and secondary star) it follows that

$$g_{TP} = \frac{n_{TP}}{4} \left[\left(\frac{m_{GP}}{m_A} \right) \left(\frac{a_{TP}}{a_{GP}} \right)^2 b_{3/2}^{(1)} \left(\frac{a_{TP}}{a_{GP}} \right) (1 - e_{GP}^2)^{-3/2} + \left(\frac{m_B}{m_A} \right) \left(\frac{a_{TP}}{a_B} \right)^2 b_{3/2}^{(1)} \left(\frac{a_{TP}}{a_B} \right) (1 - e_B^2)^{-3/2} \right]. \quad (5)$$

Note that this is an ad-hoc modification of the classical LLM. Originally, the classical secular theory is of first-order in the eccentricity and hence is valid only for low values of e_i . However, by adding the extra terms $(1 - e_i^2)^{-3/2}$ with the eccentricity dependence we can extend its range of validity. The motivation is that eq. (5) looks and behaves similar to eq. (3) with the additional terms added. In fact, [Bazsó and Pilat-Lohinger \(2017\)](#) have shown that such a modification acts as an interpolating formula between the classical LLM (in the limit $e_i \rightarrow 0$) and the Heppenheimer model (for $a_{TP}/a_i \rightarrow 0$).

Equation (5) can handle arbitrary mass ratios and is applicable for large distance ratios up to the limit $a_{TP}/a_i \rightarrow 1$, which becomes important when the giant planet approaches the outer HZ border (OHZ), but we strictly require that $a_{OHZ} < a_{GP}$. Alternatively, the LLM can be replaced by any suitable secular model that can handle at least a four-body problem, e.g. the model of [Milani and Knezevic \(1990\)](#).

2.2.3. Combined Analytical Model (CAM)

After having introduced both analytical sub-models, we now combine equations (2) and (5) to express eq. (1) in terms of the five parameters $(m_{GP}, m_B, a_{GP}, a_B, e_B)$. We assume that the eccentricity of the giant planet (e_{GP}) is small enough to neglect its effect, i.e. $e_{GP} \rightarrow 0$, which reduces the dynamical system by this variable.

In order to have a more compact notation, we introduce the following abbreviations: $\gamma_1 := m_{GP}/m_A$, $\gamma_2 := m_B/m_A$, $\alpha_1 := a_{TP}/a_{GP}$, $\alpha_2 := a_{GP}/a_B$, so that we can express $a_{TP}/a_B = (a_{TP}/a_{GP})(a_{GP}/a_B) = \alpha_1\alpha_2$. Furthermore, the eccentricity e_B appears on both sides of the equation in form of the expression $\epsilon_B := (1 - e_B^2)^{-3/2}$.

With all these definitions we can write eq. (1) for linear⁴ SR ($p = q = 1$) in terms of $(\gamma_1, \gamma_2, \alpha_1, \alpha_2, \epsilon_B)$ to obtain

$$\frac{1}{4}n_{TP} \left(\gamma_1 \alpha_1^2 b_{3/2}^{(1)}(\alpha_1) + \gamma_2 (\alpha_1 \alpha_2)^2 b_{3/2}^{(1)}(\alpha_1 \alpha_2) \epsilon_B \right) = \frac{3}{4}n_{GP} \gamma_2 \alpha_2^3 \epsilon_B (1 - \delta_g). \quad (6)$$

We will refer to eq. (6) from now on as Combined Analytical Model (CAM).

The expression for δ_g is given in eq. (4) as a function of $(\gamma_2, \alpha_2, e_B)$, where e_B appears explicitly. From now on we skip the subscript g from δ_g , and are going to use simply δ when referring to eq. (4). Note that the frequencies (mean motions) $n_{TP} = n(a_{TP})$ and $n_{GP} = n(m_{GP}, a_{GP})$ are the only dimensional quantities in this equation, and that they are known functions of the system parameters.

2.2.4. Derivation of simplified CAM

Naturally, it would be helpful to have at hand some sort of analytical expressions that allow to investigate the qualitative behaviour of the CAM solutions. These expressions are not available in general, but they can be found for an approximate form of eq. (6) that we will derive now.

The primary obstacle in eq. (6) are the Laplace coefficients $b_{3/2}^{(1)}$. We can get rid of them by assuming that the conditions $\alpha_1 \ll 1$ and $\alpha_2 \ll 1$ hold, such that we can replace these functions by their MacLaurin series expansions

$$b_{3/2}^{(1)}(\alpha) \approx 3\alpha + \frac{45}{8}\alpha^3 + \mathcal{O}(\alpha^5)$$

up to the lowest order in α . This approximation is justified because of the hierarchical nature of the dynamical system. In case of well separated orbits we expect quite small values of $\alpha < 0.1$, for

⁴ Without loss of generality we focus here on linear secular resonances, because these show the maximum effect in terms of forced eccentricities (cf. Fig. 3). In a more general setting, the coefficients (p, q) can be easily reintroduced into eq. (6) to study also nonlinear SR (see Fig. 4).

which this approximation yields relative errors of roughly 1 – 2 % compared to the values evaluated numerically from the full form of the Laplace coefficient. Deviations of this magnitude are tolerable given the inherent fit-errors of the secular model in eq. (2), that itself has median errors of 2 – 3 % relative to a fully numerical solution (compare section 3.1).

Starting from eq. (6), we replace the Laplace coefficients by their approximations, insert $n_{TP} = (Gm_A/a_{TP}^3)^{1/2}$ and $n_{GP} = (Gm_A(1 + \gamma_1)/a_{GP}^3)^{1/2}$, and eliminate common factors on both sides of the equation to obtain

$$\gamma_1\alpha_1^3 + \gamma_2\alpha_1^3\alpha_2^3\epsilon_B = (1 + \gamma_1)^{1/2}\gamma_2\alpha_1^{3/2}\alpha_2^3\epsilon_B(1 - \delta). \quad (7)$$

This equation, termed the simplified CAM, represents an approximate form of eq. (6) that shares all of its properties in the limit $\alpha_{1,2} \rightarrow 0$. Appendix B provides (approximate) analytical solutions to this simplified CAM with respect to the parameters $(\gamma_1, \gamma_2, \alpha_1, \alpha_2, \epsilon_B)$.

2.3. Properties of the CAM

We are now able to investigate the binary-star – giant planet – test planet system as a coupled dynamical problem given by eq. (6) depending on five parameters. The goal is to identify combinations of those parameters that would lead to secular perturbations inside the HZ, i.e. for $a_{\text{IHZ}} \leq a_{TP} \leq a_{\text{OHZ}}$. This knowledge is useful to exclude such systems from searches for potentially habitable planets, and allows for a quick dynamical classification of the HZ (resonant vs non-resonant).

2.3.1. Searching for CAM solutions

Our approach is to find two sets of solutions of eq. (6): in the first case for $a_{TP} = a_{\text{IHZ}}$, and in the second case by setting $a_{TP} = a_{\text{OHZ}}$. The two solutions obtained in this way mark the extremal cases where the perturbation just touches the HZ borders. For parameter values intermediate to the two identified sets the perturbation will fall somewhere into the HZ. However, one must be aware that there are circumstances for which these solutions are still too conservative. An example is that the SR falls just slightly outside of the HZ, such that our model would predict that it does not have any influence. Resonances have a certain resonance width in real systems though, this width depends on the strength of the perturbation (see, e.g. Malhotra 1998). So, if the SR were located slightly

outside the HZ and had a resonance width that is sufficiently large then it would reach into the HZ and does affect the dynamics there. Such situations must be carefully investigated on an individual basis; often numerical simulations will be necessary to decide whether or not a resonance near the HZ has an influence on it (see also [Bazsó et al. 2017](#), Fig. 2).

To simplify the search for solutions to the CAM in the five-dimensional parameter space, we fix 4 of the 5 variables and consider eq. (6) to be a one-dimensional function of the remaining variable. We then solve the equation via an iterative process, because it depends in a non-trivial way on the variables α_1 and α_2 (via the Laplace coefficients). This procedure yields parametric solutions for the selected variable as a function of the other four parameters, and the solutions can be visualized in a two-dimensional parametric space like shown in Fig. 2 and others in section 3.

2.3.2. *A motivating example*

We present as motivation a first application of the CAM in Fig. 2. In this example a binary star system is depicted that consists of a G-type primary and an M-type secondary star. The main feature is a diagonal stripe (bottom left to top right) that represents the set of parameters in the (a_B, a_{GP}) parameter space that lead to an SR in the HZ. Three specific examples serve to highlight the strength of this approach. In the first case (medium grey or orange colour) a Jupiter mass planet at 5.2 au (Jupiter’s actual semi-major axis in the solar system) would perturb the HZ if the secondary was at a distance between 60 – 80 au (see filled rectangle in the middle). The second case (light grey or yellow colour) places a Jupiter mass planet at Saturn’s position at 9.6 au, where this planet induces an SR in the HZ for stellar distances of roughly 170 – 220 au (lighter filled rectangle to the right). Another case shows the same Jupiter-mass planet at a distance of only 3 au (dark grey or purple colour) with perturbations occurring in the HZ for stellar distances between 22 – 36 au (darker filled rectangle to the left). Note that the band is artificially truncated on both ends; for $a_B < 20$ au, because such a tight binary system would require to place the GP below 2 au to maintain its orbital stability for higher secondary eccentricities, but in turn this limits orbital stability in parts of the HZ. In practice, the stripe could be traced out to much larger secondary star (and planet) distances, but the more distant the giant planet becomes the weaker its influence on the HZ would be.

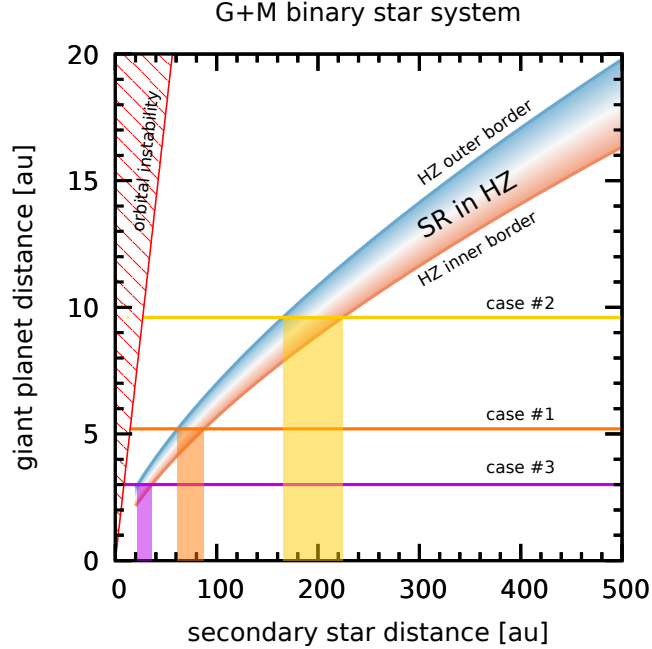


Figure 2. Along the curved diagonal strip an SR affects some part of the HZ, while in the surrounding white area there is no SR inside the HZ. The top (blue) curve marks the outer HZ border, and the lower (red) curve delimits the inner HZ border. Three example cases show parameter combinations for a fixed giant planet distance (horizontal lines): 5.2 au for case 1 (orange), 9.6 au for case 2 (yellow), or 3.0 au for case 3 (purple). For each example a certain range of secondary star distances (coloured boxes) induces an SR in the HZ. The hatched area on the left margin indicates the critical distance beyond which orbital instability of the planet is expected.

2.3.3. *Effect of a secular perturbation in the HZ*

Apart from being able to locate and identify secular perturbations some important questions remain: How much does it matter? Would potential planets in the HZ even care about such perturbations? The answer is likely yes! To understand the reason, we need to consider the driver of habitable conditions: the stellar irradiation.

It became evident from the investigations of [Eggl et al. \(2012\)](#), [Kaltenegger and Haghighipour \(2013\)](#), [Cuntz \(2014\)](#), and others that a static definition of habitable zones in binary star systems is only a rough approximation, and for some applications it is unjustified. The gravitational interaction of the (at least) three bodies results in quasi-periodic oscillations of the planet’s eccentricity even for

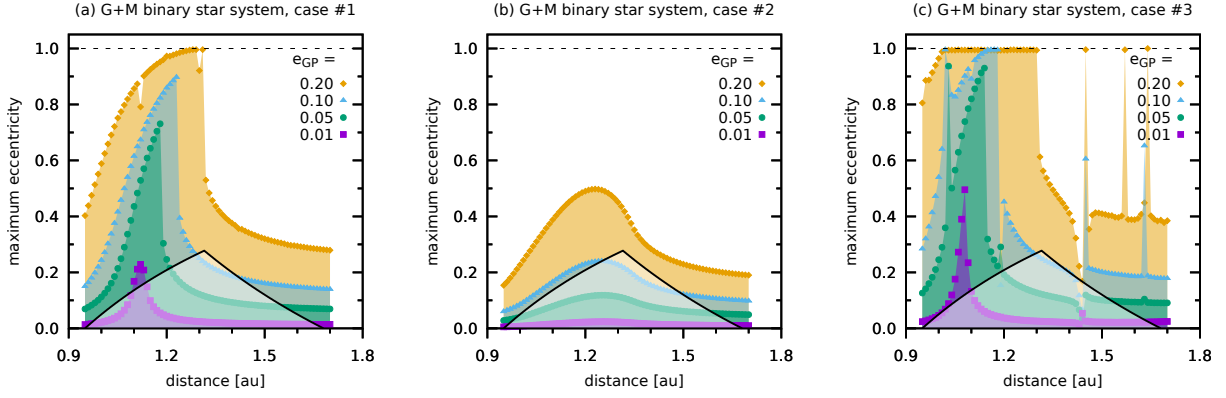


Figure 3. Maximum eccentricities of test planets distributed across the HZ. The y -axis gives the maximum value of the eccentricity (max- e) over the simulation time span of 2 Myrs. Different symbols (and colours) distinguish specific initial eccentricities of the perturbing giant planet. The broad peak in max- e in each panel corresponds to the location of the linear SR with the GP; narrower peaks represent locations of MMR. Panels (a)–(c) refer to the respective example cases 1–3 from Fig. 2. A triangle-like overlay indicates the permanent HZ as a function of the test planet’s eccentricity.

initially circular planetary orbits. These oscillations in eccentricity are correlated with phases of larger amplitude variations in irradiation. Consequently, a planet that may sustain habitable conditions on a low eccentricity orbit could leave the permanently habitable zone (PHZ) for a temporarily increased eccentricity – just to return to a moderate eccentricity some time later. It is this effect on the eccentricity that effectively limits the habitability.

In Fig. 3 we provide the results of calculations for (massless) test planets distributed across the HZ for the three cases from Fig. 2. These fully numerical simulations were performed with the N-body code Mercury (Chambers 1999) using the adaptive time-step Radau method with local error tolerance 10^{-12} . Each figure shows the maximum eccentricities (max- e) of test planets as a function of their initial location. The max- e is color coded according to four different scenarios related to the giant planet’s orbital eccentricity (from bottom to top): (1) $e_{GP} = 0.01$ (square symbols), (2) $e_{GP} = 0.05$ (circles), (3) $e_{GP} = 0.1$ (triangles), and (4) $e_{GP} = 0.2$ (diamond symbols). Panel (a) for case 1 refers to the giant planet at 5.2 au, in panel (b) the planet is located at 9.6 au, while in panel (c) the planet is at 3.0 au. A triangle-shape overlay (in light gray) delineates the region of the PHZ for the

test planets. Any test planet that acquires a max-e value outside of this region must be considered uninhabitable (at least temporarily).

In the first example case the perturbing giant planet causes a linear SR near 1.1 – 1.2 au that is marked by the spikes in max-e. Even for $e_{GP} = 0.01$ the GP forces test planets locally to max-e values of 0.2. An increase of e_{GP} to 0.05 then boosts the eccentricities to values beyond 0.6. In these latter cases some small intervals with moderate max-e remain, e.g. from 1.2 – 1.55 au (1.3 – 1.4 au) for $e_{GP} = 0.05$ (0.1), respectively. For even higher e_{GP} no test planet can maintain max-e values low enough to stay in the PHZ; some even escape from the system on unbound trajectories.

The second example with a more distant GP in panel (b) exhibits a linear SR at about the same location as before. The spike in max-e is not as pronounced as in the other example, but it is still visible even for relatively small e_{GP} . An increase in e_{GP} first leads to the deterioration of habitability near the edges of the HZ, but increasingly also in the inner regions. For $e_{GP} = 0.1$ already many test planets achieve too high max-e values and only in an interval from 1.25 – 1.5 au they would remain permanently habitable; for an even more eccentric GP no habitable test planet remain any more.

Case 3 in panel (c) represents a strongly perturbed HZ by a GP at a distance of only 3 au. Besides the main linear SR at about 1.1 au also numerous narrow peaks appear that correspond to MMR with the GP, see Table 2 for a list of MMR. The width and max-e amplitude of the SR are strongly modified when increasing the GP’s eccentricity, such that for $e_{GP} > 0.1$ no habitable test planets remain. Note that apparently the 5:1 MMR has the largest effect (max-e > 0.9 already for $e_{GP} \geq 0.05$), while the theoretically stronger 3:1 and 5:2 MMR are visible only for $e_{GP} = 0.1$ or higher. Although the 5:1 MMR is a fourth order MMR, here it interacts with the SR and becomes the dominant MMR locally, apart from the 2:1 MMR that is located slightly beyond the right edge of this figure.

These examples show clearly that the GP’s eccentricity plays a crucial role for secular perturbations in the HZ. It is obvious that slight variations in e_{GP} can result in large perturbations that involve the large forced max-e of the TP induced by low to moderately eccentric GP, and the feedback effects on e_{GP} discussed in section 3.2.3.

Table 2. A selection of relevant MMR in the HZ for $a_{GP} = 3$ au (case 3).

MMR	Location [au]
5:1	1.03
9:2	1.10
17:4	1.14
4:1	1.19
3:1	1.44
8:3	1.56
5:2	1.63
2:1	1.89

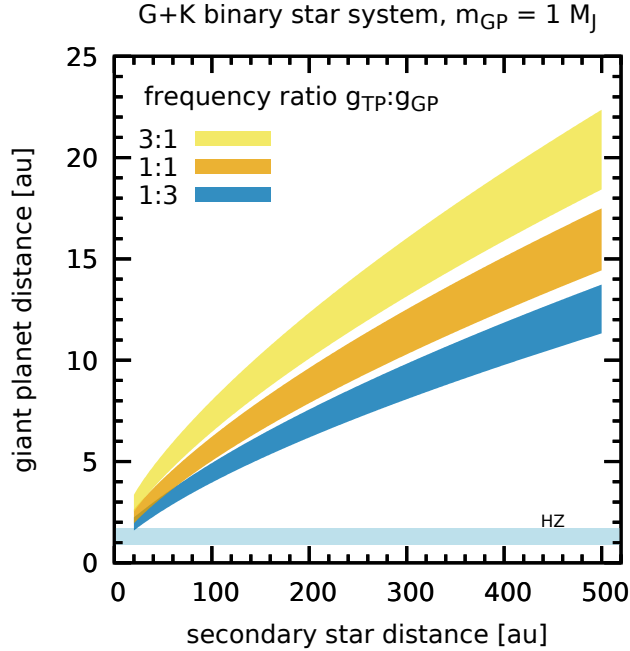
**Figure 4.** Examples of nonlinear SR locations identified via CAM. From top to bottom the shaded bands represent the following SR: the $g_{TP} - 3g_{GP}$, $g_{TP} - g_{GP}$ (linear), and $3g_{TP} - g_{GP}$. The horizontal stripe at the bottom represents the habitable zone.

Figure 4 depicts a binary star system with a K-type secondary ($m_B = 0.7 M_\odot$) and the bands of various SR. Besides the linear SR (middle curve) the figure also shows the $(q, p) = (1, 3)$ (top curve)

and $(q, p) = (3, 1)$ (bottom curve) nonlinear SR. Note that the vertical width of the curves in a_{GP} does not indicate their strength (nonlinear SR are rather weak, cf. Fig. 7), but rather the feasible range of GP distances that induce these SR in the HZ. At small secondary star distances these three curves overlap which means that two (or more) SR may appear simultaneously in the HZ.

3. RESULTS

In a first part (section 3.1) we assess the analytical model’s accuracy (i.e. the predicted secular frequencies g_{GP} and g_{TP}) relative to numerical reference results, while in section 3.2 we apply the CAM to different binary systems and present the effect of varying different system parameters.

3.1. Model accuracy

As the full CAM consists of two models we check the performance of each of them independently. Section 3.1.1 contains the checks related to the CAM and g_{GP} , while section 3.1.2 contains results pertaining to the g_{TP} part. Additionally, we compare the results of the full CAM (eq. (6)) to those of the simplified CAM (eq. (7)) in section 3.1.3.

3.1.1. Accuracy of full CAM: GP frequency

We performed a series of test computations on a two-dimensional grid in the (a_B, e_B) parameter space for four different masses of the secondary star. The main goal was to assess the accuracy of the analytical model in eq. (2) when its assumptions of zero mass and eccentricity for the GP are not met. In fact, we tested several different GP masses and non-zero eccentricities for a total of more than 14,000 test runs. The simulations were done in the framework of the full three-body problem, purely Newtonian gravity, and the equations of motion were solved with the Radau method from the Mercury package (Chambers 1999). The secular periods vary over several orders of magnitude (roughly $10^3 - 10^7$ years) in the parameter range of interest, so we made sure to cover a simulation time of at least 20 secular periods (estimated from eq. (3)) and to obtain at least 2000 data points for the time evolution of the heliocentric orbital elements. Each of these individual test runs was subject to a frequency analysis to obtain a reference value for g_{GP} . The reference frequency was obtained by the

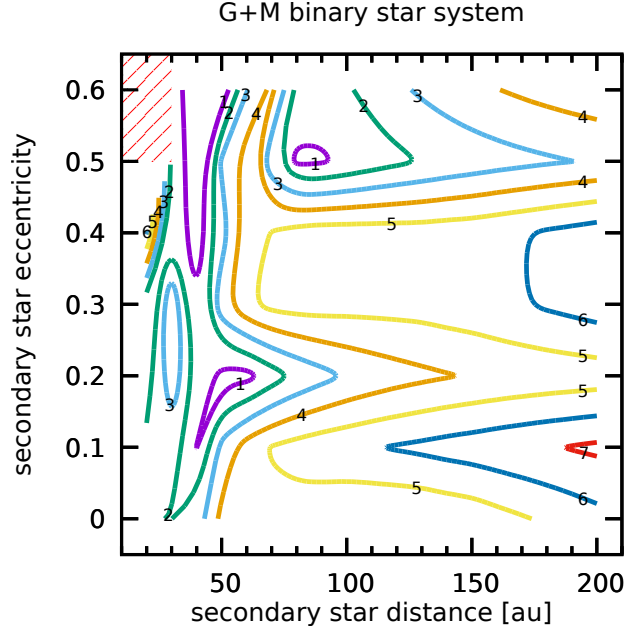


Figure 5. Comparison of the deviations between the analytical model in eq. (2) and results from fully numerical simulations for a G+M binary star system. The contour lines trace the relative errors (in percent) of the giant planet’s precession frequency g_{GP} . In the top left corner (hatched area) the giant planet’s orbital instability precludes a comparison.

FMFT method (Šidlichovský and Nesvorný 1996; Laskar 1999) from the time series of the complex variable $z(t) = h(t) + ik(t)$, where $i = \sqrt{-1}$, with $h(t) = e(t) \sin \varpi(t)$ and $k(t) = e(t) \cos \varpi(t)$.

Figure 5 displays a comparison of the CAM and the numerical reference values. The contours show the relative error in percent for the case of an M-type secondary, where the giant planet is located at 3 au on an initially circular orbit. In this case the agreement is very good, with a maximum deviation of less than 8 %. Generally, we observe the largest errors in the top-left corner for tight and highly eccentric secondaries, where orbital instability of the GP becomes an issue (cf. hatched area). When increasing the giant planet’s mass to $5 M_J$ also the maximum error increases to ~ 30 %, while the average error stays below 10 %.

We show a more global comparison in Fig. 6, that gives an overview on the statistical distributions of the relative errors for the four secondary star masses. For this figure we selected the subset of the simulations with $m_{GP} = 1 M_J$ and distances a_{GP} of 3, 5, and 7 au. The vertical axis shows that the

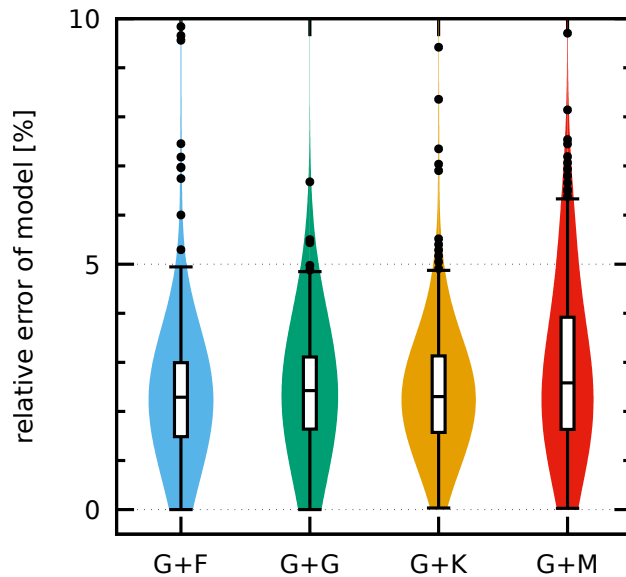


Figure 6. Overview of the relative error (on the y -axis) between the analytical model and fully numerical simulations for all four binary cases. The boxes represent the range in between the first and third quartiles, with a horizontal line at the median value. The errorbars indicate the range that spans 95 % of all points in the data set; outlying points beyond these limits are visible as black dots at larger errors. Shaded regions show the normalized frequency distribution of data points obtained via a kernel density estimate using Gaussian kernels.

relative errors are usually quite small with only few exceptions. For each of the four cases a boxplot indicates the range of errors in between the first and third quartiles, horizontal lines represent the median values that lie around 2.5 % in all cases. Furthermore, the region enclosed by the errorbars contains 95 % of the data points, while black dots mark individual outliers. The normalized frequency distributions of data points are shown as shaded regions. It is thus clearly visible that the distributions are all unimodal and that in > 95 % of cases the analytical model deviates by less than 10 % from the numerical reference value. The remaining outliers stem mainly from those simulations that combine a highly eccentric and tight secondary with a more distant giant planet. These edge cases lie close to the instability border (see top left corner in Fig. 5) and are characterized by large values of α_2 .

3.1.2. Accuracy of full CAM: TP frequency

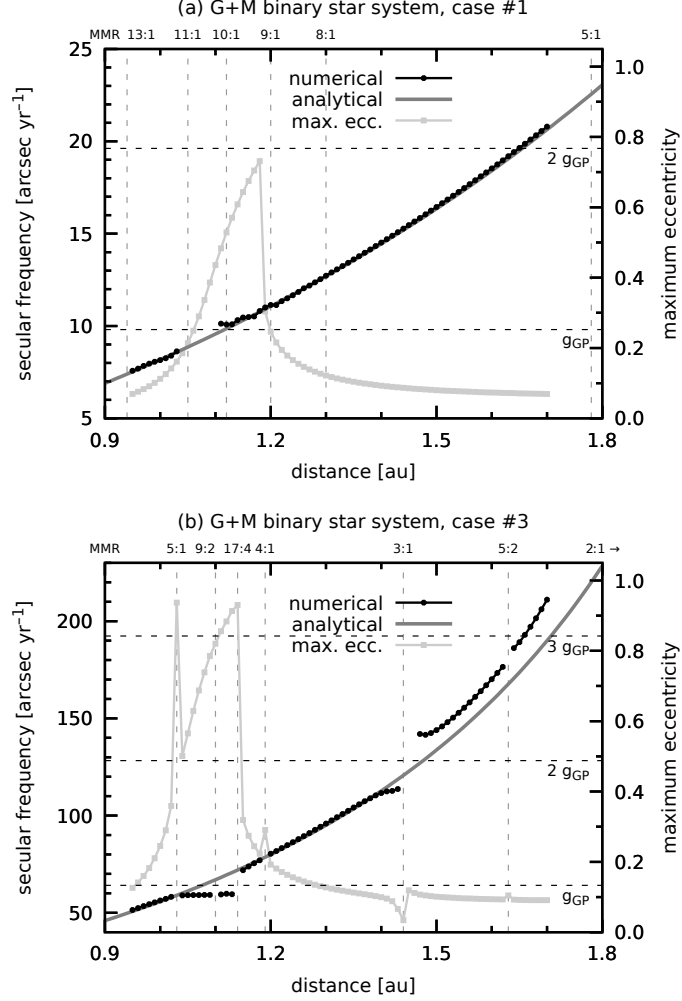


Figure 7. Comparison of secular frequencies obtained from the analytical model in eq. (5) with frequencies from fully numerical simulations for two G+M binary star systems. Panel (a) corresponds to case 1 from Fig. 2 with $a_{GP} = 5.2$ au, while panel (b) is for case 3 with $a_{GP} = 3$ au; initially $e_{GP} = 0.05$ in both cases. The solid grey lines show the analytical frequencies overplotted with black dots for the numerical frequency values (left y -axis). As a visual aid we replot the respective max-e curves (light grey squares, right y -axis) from Fig. 3. Vertical dashed lines indicate locations of MMR.

A second set of test simulations covers eq. (5). The aim is to assess how well this equation performs relative to numerical reference results in the presence of two massive perturbers. All simulations are performed in a restricted four-body problem with the Radau method (see section 2.3.3 for details) and cover a duration of 2 Myr, with output every 100 years in order to resolve short period variations in eccentricity. We obtain the reference frequencies again with the FMFT method.

Figure 7 presents the comparisons for two sample cases. Panel (a) shows case 1 from Figs. 2 and 3, where we have $a_{GP} = 5.2$ au, $e_{GP} = 0.05$, and $e_B = 0.01$. The solid grey curve gives the secular frequencies as predicted by eq. (5) (left y -axis). Black dots represent numerically determined apsidal precession frequencies for test planets in the HZ range (0.95 – 1.70 au). We overplot the max-e curve (with light grey squares, see values on the right y -axis) to aid the identification of relevant features. Horizontal dashed lines indicate the GP’s proper precession frequency (g_{GP}) and multiples of its value, whereas vertical dashed lines indicate MMR (see respective labels at the top). It is visible that there is an excellent agreement between the analytical and numerical frequencies, except for the interval between the 11:1 and 10:1 MMR. The nominal linear SR location is at 1.12 au where the grey curve equals g_{GP} ; the nonlinear SR $g_{TP} - 2g_{GP} \approx 0$ lies near to 1.65 au. According to the numerical data it seems that the exact SR location is slightly shifted to smaller distance ($\lesssim 1.1$ au). Note that the peak in max-e does not coincide with the location of the SR, moreover it is asymmetric with a sharp edge short of the 9:1 MMR. A similar qualitative behaviour has also been demonstrated for secular resonances in the solar system (Malhotra 1998, Fig. 3). The max-e curve is more symmetric for low GP eccentricity (cf. Fig. 3), but the asymmetry becomes more pronounced with increasing e_{GP} .

The second panel (b) depicts case 3, with the same parameters as above except for $a_{GP} = 3$ au. Again the light grey points represent the max-e values for individual test particles, where we now have several narrow peaks due to MMR besides the dominating broad SR. The analytical and numerical frequencies are in rather good agreement, except at locations of MMR and starting from about 1.5 au outwards to larger distances. A main cause of this disagreement is the influence of the strong 2:1 MMR at 1.89 au (outside of the plot range). The analytical model in eq. (5) only accounts for secular terms of the disturbing function, but here also the resonant (short period) terms play an increasingly important role. An estimate of the libration width of the 2:1 MMR gives $\delta a \approx 0.06$ au (Malhotra 1998; Murray and Dermott 1999), but this is not wide enough to reach into the HZ, as we can also see from the flat part of the max-e curve at distances larger than 1.5 au. The width of the linear SR (at 1.1 au) roughly corresponds to the interval between the 5:1 and 17:4 MMR, compare Tab. 2 for

their exact locations. In this region the test planet’s proper precession frequency does not change. A similar behaviour occurs near the 3:1 MMR that falls into the vicinity of the $g_{TP} - 2g_{GP}$ nonlinear SR. Such flat parts (or plateaus) of the frequency curve correspond to crossing of resonance islands, as demonstrated for different MMR in [Robutel and Laskar \(2001, Fig. 1\)](#). Another interesting case is the 3:1 MMR, where the max-e curve shows a ‘pulse-like’ effect. [Christou and Murray \(1999\)](#) found a similar behaviour when they analysed the effect of near MMR on the secular precession frequency. An explanation for the pulse is that the secular frequency profile is modified by the sign-change of the MMR’s small divisor, which – in case of second-order MMR – gives a negative contribution before the resonance and a positive one afterwards. This effect on the secular frequency directly relates to the max-e curve where it is visible, too.

In general, missing data points in [Fig. 7](#) indicate a complex dynamical behaviour of the respective particle, where the FMFT was unable to determine a unique dominating frequency. Note that in a purely secular setting the d’Alembert rules require additional frequencies (like nodal precession frequencies) to satisfy the resonance relation in [eq. \(1\)](#) for a nonlinear SR. Alternatively, a nonlinear SR may couple with a nearby MMR to fulfill the exact resonance condition, such as for the $(p, q) = (2, 1)$ SR and the 3:1 MMR. This coupling gives rise to the max-e peaks visible in [Fig. 3 \(c\)](#) for $e_{GP} \geq 0.1$, but also a local minimum in max-e is associated to the same 3:1 MMR. The presence of SR and nearby MMR does not necessarily lead to adverse effects, because MMR can also have a stabilizing effect. One particular example was shown in [Pilat-Lohinger \(2005, Fig. 1\)](#) for the γ Cephei system, where a stable island around the 3:1 MMR (near to an SR) persists also for non-coplanar motion up to an inclination of 15° relative to the GP.

Overall, [Figs. 3 and 7](#) clearly show that the linear SR is the dominant perturbation and that higher order SR play a secondary role. This finding is backed-up by the results of [Bancelin et al. \(2016, Fig. 3\)](#) whose max-e plots also show a dominant linear SR that locally couples to various MMR. Nonlinear SR become relevant for much higher e_{GP} when the resonance widths of SR and MMR are wide enough to overlap and cause extended regions of chaotic motion. Such an example was

presented in Bazzó et al. (2017) for the HD 196885 system⁵ where the nonlinear SR $2g_{TP} - g_{GP}$ and $3g_{TP} - g_{GP}$ overlap with nearby MMR. For another example of nonlinear SR see Fig. 4.

3.1.3. Accuracy of simplified CAM

Figures 5 and 6 demonstrate that the full CAM provides an accurate description of the secular dynamics. The open question is how well the simplified CAM reproduces results of the full equation.

A first test is shown in Fig. 8 (a). The plot uses eq. (B1) to express the dependence of the mass ratio γ_1 on the secondary star distance (via α_2). It shows two shaded regions that overlap each other partially. The darker shade represents the solutions according to the simplified CAM, while the lighter shade are the results from the full CAM. Apparently the simplified CAM shows the same qualitative behaviour and follows the full solutions closely, but with an offset in vertical direction (note the logarithmic scale of the y -axis). This deviation does not show any dependence on the secondary star distance (i.e. α_2) or on the secondary star's eccentricity (not shown). We have to bear in mind that eq. (B1) involves strong approximations with respect to the distance ratios α_1 and α_2 . Accordingly, the major effect causing the visible deviation is the magnitude of α_1 (fixing $a_{GP} = 5.2$ au). The deviation becomes larger with increasing distance ratio α_1 , i.e. when the GP is near to the HZ and its perturbations are stronger.

Figure 8 (b) shows another comparison of the accuracy. In this case we use eq. (B4) to trace the distance ratio α_2 as a function of secondary star mass in the range $0.08 \leq m_B \leq 2.1 M_\odot$. We set the giant planet to 5 au and always assign an eccentricity of $e_B = 0.25$ to the secondary. The results demonstrate that the simplified CAM is able to reliably describe the dynamics, albeit with a small deviation. It is visible from the figure that the simplified CAM retrieves a narrower region in the parameter space than the full CAM, but the deviation is only minor especially at the lower border. Similar to the first test case the parameter α_1 plays a major role for the magnitude of the deviation: the larger α_1 the larger is the deviation.

⁵ Radial velocity observations of the system suggest an exoplanet with minimum mass $3 M_J$ and eccentricity $e_{GP} \sim 0.5$.

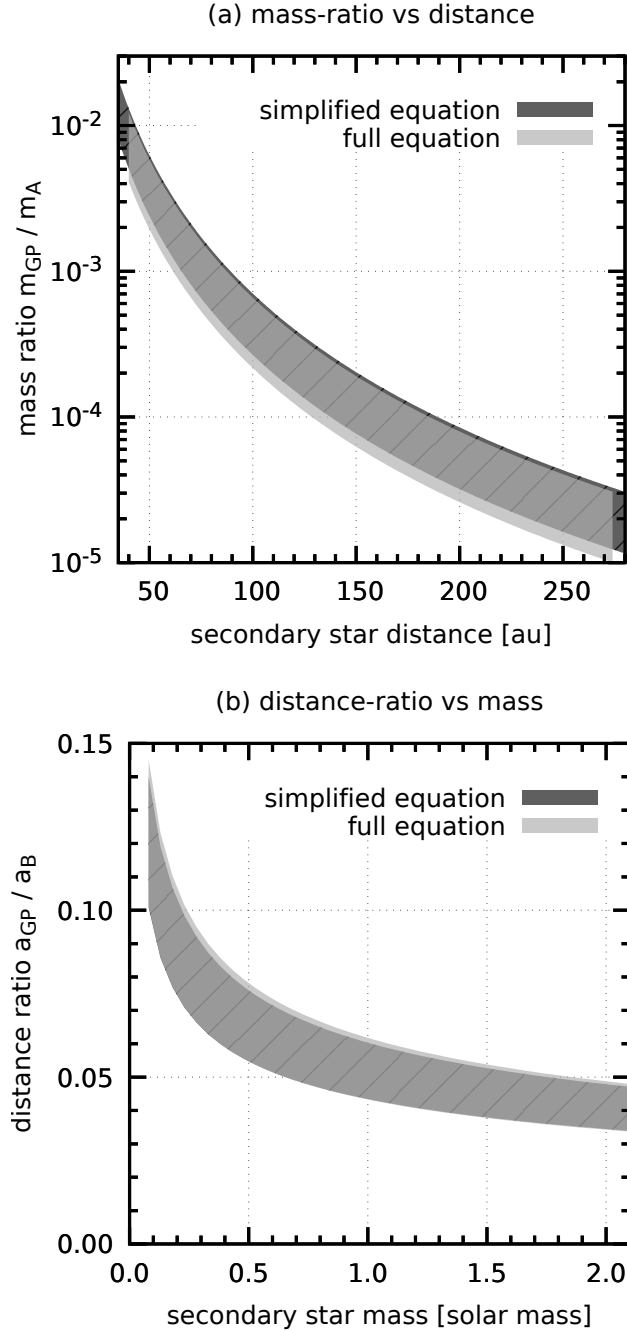


Figure 8. Comparison of model accuracy between simplified CAM (darker colour with pattern in the background) and full CAM (lighter colour). Panel (a) shows the mass ratio γ_1 as a function of secondary star distance for a G+M binary on circular orbits. The plot in panel (b) shows the distance ratio α_2 as a function of secondary star mass for a Jupiter-mass planet at 5 au. Note that the curves overlap each other at the bottom border, but the curve for full CAM is slightly more extended at the upper border.

We can conclude that the simplified CAM is able to reliably describe the dynamics, provided that the giant planet does not approach the HZ too closely. Its limitations are clearly connected to the parameter $\alpha_1 = a_{TP}/a_{GP}$ that should be $\alpha_1 < 1/3$ (in particular < 0.1) in order to avoid the effect of MMR that would invalidate a purely secular model. The approximate solutions can thus serve to quickly estimate the variation in any of the five system parameters, and to scan a large parameter space for a first overview on possible secular perturbations in the HZ.

3.2. Application to exoplanet systems of binary stars

Before continuing to present the model outcomes applied to synthetic systems, we need to be more explicit about the choice of system parameters. As mentioned above, we consider only perturbers external to the HZ of a G-type main sequence star. This puts a constraint on the location of the giant planet to orbit beyond about 2 – 3 au depending on its eccentricity. Thus, in a first step, we need to get an overview of suitable exoplanet candidates.

3.2.1. Selection process

We selected from various online catalogs⁶ all confirmed exoplanets that fulfill the following two criteria: (1) masses between 0.1 – 10 Jupiter masses (M_J), and (2) semi-major axes between 2 and roughly 10 au, irrespective of planet or stellar multiplicity. This gives a total of 220 exoplanets in our sample. The choice of parameters is motivated first by the evident incompleteness of planet detections at larger distances, and second by the survey of Bryan et al. (2016). From their combined radial velocity – imaging survey those authors concluded that the frequency of giant planets peaks between 3 and 10 au for the mass range up to 20 M_J .

Figure 9 shows the scatter plot and respective parameter distributions of these exoplanets. The histogram on the right shows that the median (minimum) mass is around 2.5 M_J , with an extended tail reaching up to the selection limit. The distribution of semi-major axes in the bottom histogram is more concentrated to lower values, with about 90 % of the sample having values of $a_{GP} \leq 6$ au.

⁶ For instance, The Extrasolar Planets Encyclopaedia of Schneider et al. (2011) at <https://exoplanet.eu/catalog/>, or the NASA Exoplanet Archive <https://exoplanetarchive.ipac.caltech.edu/index.html>.

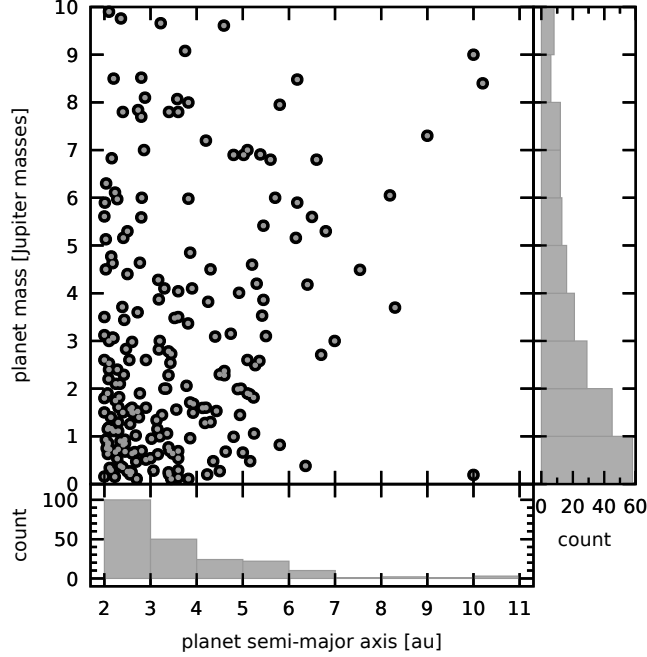


Figure 9. Sample of 220 confirmed exoplanets from the Exoplanet.eu database. The selected planets are restricted to masses in the interval from 0.1 to 10 Jupiter masses, and semi-major axes from 2 to 11 au. The histograms show the distributions of the respective parameter.

This is a consequence of the detection by mainly radial velocity surveys that favour exoplanets with shorter orbital periods (Cumming et al. 2008; Perryman 2011).

This selection of giant planet properties has implications on the secondary star parameters. We restrict ourselves to masses in the interval $0.4 \leq m_B \leq 1.3 M_\odot$ (roughly spectral types M2V – F5V), and a lower limit on the stellar separation of $a_B \geq 20$ au. The eccentricities can vary between $0 \leq e_B \leq 0.6$ according to the fit limitation in the model of Andrade-Ines and Eggl (2017).

3.2.2. Binary star parameters

As we can appreciate from eq. (6) the right-hand side has a non-linear dependence on γ_2 , α_2 , and e_B . This means that the location of the SR will strongly depend on the secondary star’s parameters. We will first investigate the qualitative behaviour of the solutions.

In a former study, Pilat-Lohinger et al. (2016) have investigated the system HD 41004 AB as a proxy for binary stars with circumstellar exoplanets. They have demonstrated that the positions of SR are connected to the orbital parameters of the secondary star, especially to its distance. Accordingly,

they have investigated the qualitative behavior of SR location for a shift in a_B (for $a_{GP} = \text{const.}$). Here, our purpose is different: We constrain the SR to lie in the HZ and show how the system parameters (masses and distances of GP and secondary) need be coupled in order to maintain that situation.

From Fig. 2 we can observe the correlation between a_B and a_{GP} that results in the diagonal stripe. This means that for each value of a_B (for fixed a_{TP}) there is a unique solution to eq. (1) that yields a distance a_{GP} causing an SR in the HZ. The figure contains another important detail: When increasing the secondary's distance from the host star (for fixed GP distance along the horizontal lines, from left to right) we can observe that the SR moves from outside in. This means that first the outer part of the HZ (upper edge of the stripe) would be affected, then some intermediate region of the HZ, and finally the inner border (lower edge). Increasing the distance even more would then remove the SR from the HZ and would place it closer to the host star. Such an inverse relation between a_B and the SR location is not immediately obvious from eq. (6), but we can understand it in terms of α_2 . The variable α_2 is simply the ratio a_{GP}/a_B , hence it is inversely proportional to the secondary's distance. In case that the other parameters are held fixed (as in Fig. 2), an increase of a_B leads to a decrease of g_{GP} because of the term $\propto \alpha_2^3$, cf. eq. (3). Conversely, the frequency g_{TP} also has to decrease to satisfy eq. (6). The balance is restored through the term $\propto \gamma_1 \alpha_1^2$ (that is a monotonic function and generally dominates over the second term) via the decrease of α_1 , i.e. the resonance location moves away from the giant planet and closer to the host star. A physical interpretation of this behaviour is that a more distant perturbing secondary star reduces the rate of angular momentum exchange with the giant planet – its secular frequency g_{GP} decreases. Similarly, test planets have lower orbital precession frequencies the further away they are from the GP (which is their main perturber), such that necessarily the resonance location moves away from the GP.

At the left edge of the Fig.2, the red line denotes the critical distance, a_{crit} , of the GP according to the fits of Holman and Wiegert (1999) and Pilat-Lohinger and Dvorak (2002). This line separates the dynamically unstable area (hatched, to the left) from the region of orbital stability. The indicated example with $e_B = 0$ is an optimistic best-case scenario, typically the secondary star has a non-zero

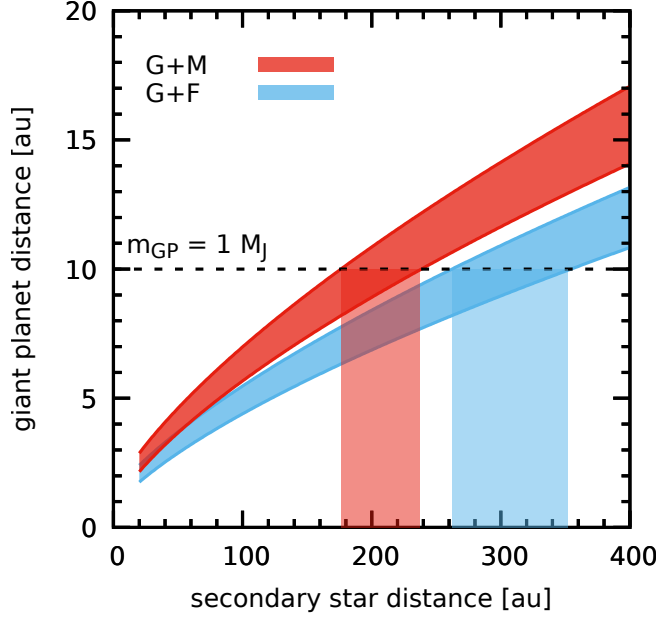


Figure 10. Resonance locations as a function of the secondary star’s mass. These two cases show a G+M binary (top curve), and a G+F binary (bottom curve). The corresponding rectangles show secondary star distances (for a GP at 10 au) that perturb the HZ.

eccentricity. Furthermore, the results of [Pilat-Lohinger and Dvorak \(2002\)](#) suggest that the hatched region would also be more extended if we accounted for the GP’s elliptic motion.

One of the main observables of binary star systems is the mass of the secondary star. This parameter is of utmost importance to dynamical studies, because it contributes significantly to the size of the host star’s region of orbital stability and determines the strength of gravitational perturbations. In the following example we show the variation of the SR’s location with the secondary star’s mass.

Figure 10 presents two binary stars in the same parameter space like before. The G+M (upper curve; $m_B = 0.4 M_\odot$) and G+F (lower curve; $m_B = 1.3 M_\odot$) systems relate to edge cases with lowest and highest secondary star masses, respectively. All other mass combinations (e.g. G+G, G+K) fall in between these two curves. In this example there is a giant planet with one Jupiter mass at 10 au (dashed horizontal line). This planet induces an SR in the HZ for secondary star distances of 180 – 240 au in the G+M case, and 260 – 350 au in the G+F case. There is a clear trend with

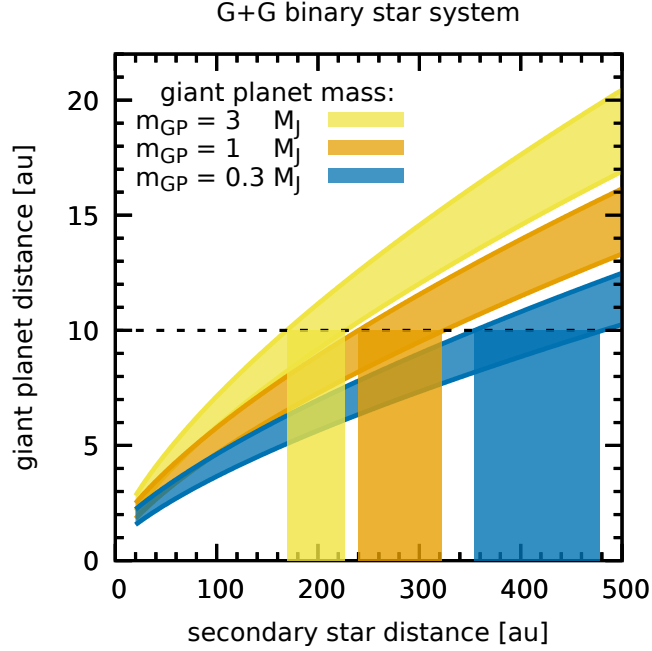


Figure 11. Resonance locations as a function of the GP’s mass. The plot shows a G+G binary star system for three different GP masses (in Jupiter masses, M_J). The GP is always at a distance of 10 au (dashed line).

secondary mass: the curve becomes flatter with increasing mass, and the absolute width (in terms of a_B) of the SR generating region broadens.

We can thus derive a general picture from Figs. 2 and 10: (1) there is a positive correlation between giant planet and secondary star distance for fixed secondary star mass; and (2) the secondary’s mass directly relates to the interval of stellar distances generating SR for fixed giant planet distance. This means that a higher mass secondary at a distance of several hundreds of astronomical units might still perturb the GP in such a way as to induce an SR in the HZ.

3.2.3. Binary star and planet parameters

Until now some planet-related parameters were held constant or ignored altogether. Next we will consider also the variation of these planet parameters and investigate their influence on the results.

We have already demonstrated in Fig. 10 that there is a correlation of stellar mass and resonance location. A similar correlation also exists for the planet mass, although with the inverse effect as Fig. 11 shows. This figure displays the same parameter space (a_B, a_{GP}) like the ones before. In this

example we have a couple of G-type stars (each with $1 M_{\odot}$) with a planet located at 10 au whose mass is a free parameter. The top curve is for a planet with 3 times the mass of Jupiter (M_J), the middle curve for $1 M_J$, and the bottom curve corresponds to a Saturn-mass planet. As the GP's mass increases (from bottom to top) the curve becomes steeper and the resonance location shifts to the left towards smaller secondary star distances. The consequences of this behaviour for different planet masses are twofold: (1) a negative feedback for more massive planets, and (2) a feedback through coupling of planetary mass and eccentricity. To clarify both issues we will compare two systems for equal planetary distances but with different masses.

It is intuitively clear that a more massive planet is a more efficient perturber of the HZ area than its lower mass counterpart. However, at the same time, a higher mass planet also requires smaller stellar distances to force the SR into the HZ, as it is visible from the figure. These two facts entail stronger perturbations in the HZ due to larger planet mass and closer secondary star. Hence, the negative feedback consists in an increased perturbation strength for a higher mass planet in combination with a closer secondary star.

The second feedback effect concerns the opposite effect. With decreasing planet mass the perturbing secondary star has to shift outwards to a distance of several hundred au to place an SR into the HZ. Such extended systems have a weaker dynamical coupling than more compact ones, hence one would not expect strong perturbations in the HZ. However, the giant planet's eccentricity plays a crucial role and compensates for the weaker coupling to the secondary star, see Fig. 3 (b). In a wide binary system the second star is more susceptible to external perturbations e.g. from passing stars (see section 4.1). Such perturbations can act to increase the secondary star's eccentricity. The giant planet's forced eccentricity is approximately $\propto e_B/(1 - e_B^2)$ (see [Andrade-Ines and Eggl 2017](#)), so it increases with larger e_B . Additionally, in former studies we have found that observed exoplanets have higher eccentricities in general than what their forced eccentricity would suggest (see [Bazsó et al. 2017](#), Table 1). Although the secondary star must be farther away for lower mass planets it can effectively induce a higher planetary eccentricity. In this way the increased eccentricity can balance the magnitude of perturbations that otherwise would decrease with smaller planetary mass.

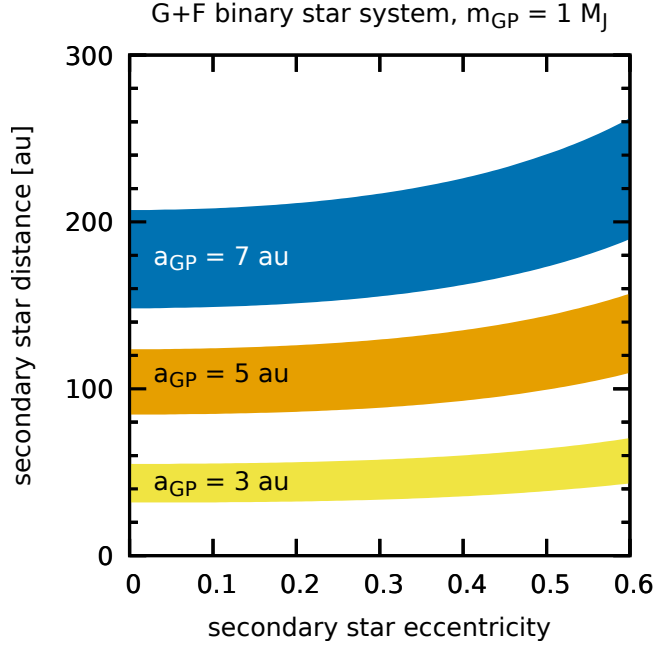


Figure 12. Resonance locations as a function of the secondary star eccentricity and giant planet distance. The perturbed zone falls to different locations depending on the giant planet’s distance. This zone also shifts depending on the secondary star’s eccentricity.

The eccentricity does not only play a role for the planet, but – more importantly – also for the stellar orbit. Figure 12 shows a different cut through the (e_B, a_B) parameter space. Three cases present the resonance location as a function of the secondary’s eccentricity and the planet’s location (here the GP has one Jupiter mass). When placing the GP to 3, 5, or 7 au (from bottom to top), respectively, the SR is induced by secondaries in a wide range of distances (y -axis). The SR location also depends on the secondary star eccentricity: as e_B grows the SR moves outwards with respect to the circular case. We can identify the cause for this variation with the terms $\propto (1 - e_B^2)^{-3/2}$ in eq. (6). These two terms are responsible for the weak deviation from the circular value at low e_B , and the increasingly larger difference at high e_B .

A striking characteristic of this figure pertains to the large shifts in a_B for a minor change of a_{GP} . For instance, the SR is displaced from about 50 au (for $a_{GP} = 3$ au) to roughly 200 au (for the GP at 7 au). These results indicate potentially dramatic changes of the system’s secular architecture by slight shifts in a_{GP} (see section 4.1).

3.3. Resonance generating distance of giant planet

In Figures 2, 10, and 11 we can observe that the distances of GP and secondary star show a positive correlation, but also that this relation is basically nonlinear. It is very important to understand the occurrence of SR in the HZ as a function of the GP's semi-major axis, a_{GP} , for actual applications. Hence, we need to understand the relation between a_{GP} and a_B as a function of the other parameters. For this we cannot use the solutions presented in Appendix B.4, because they express α_2 in terms of α_1 which itself contains a_{GP} , so those equations only give implicit relations. Conversely, in the following we will derive an explicit relation on the basis of eq. (7).

We start from the simplified CAM in the limit $\delta \rightarrow 0$ to get rid of the additional dependence on α_2 . Recall the definitions $\alpha_1 = a_{TP}/a_{GP}$ and $\alpha_2 = a_{GP}/a_B$, and that the constant a_{TP} is either a_{IHZ} or a_{OHZ} for the inner or outer HZ border, respectively. After inserting the corresponding variables into eq. (7), we obtain a cubic equation for $z = a_{GP}^{3/2}$. The general solution is thus given by

$$\alpha_2 = 3^{-2/3} \left(\frac{a_{TP}}{a_B} \right) \left(\frac{(u + u^{-1} - 1)^2}{1 + \gamma_1} \right)^{1/3}, \quad (8)$$

with the abbreviations

$$u = \left(-2c_2^3 - 27c_0c_3^2 + 3\sqrt{3}\sqrt{4c_0c_2^3c_3^2 + 27c_0^2c_3^4} \right)^{1/3} / (2^{1/3}c_2),$$

and $c_0 = -\gamma_1 a_B^3$, $c_2 = -\gamma_2 \epsilon_B$, $c_3 = (1 + \gamma_1)^{1/2} \gamma_2 \epsilon_B a_{TP}^{-3/2}$.

An important property of solution (8) is that the expression $\gamma_2 \epsilon_B$ appears only in this form, i.e. these parameters are never separated from each other. Furthermore, we could expand the denominator into a power series $(1 + \gamma_1)^{-1/3} \approx 1 - \gamma_1/3 + O(\gamma_1^2)$ since $\gamma_1 = m_{GP}/m_A \ll 1$. Note that the ratio a_{TP}/a_B also plays a role in u via c_0c_3 .

Equation (8) is useful to calculate the orbital distances of GP that would generate secular perturbations in the HZ for any given binary star system. Once the corresponding value of α_2 is known, we can determine the GP location from $a_{GP} = \alpha_2 a_B$ and construct parametric plots like in Fig. 2.

Tables 3 – 6 in Appendix C serve to assess the accuracy of eq. (8). Each table lists the critical values $\alpha_{2,\text{IHZ}}$ and $\alpha_{2,\text{OHZ}}$ (for the inner and outer HZ border, respectively) for a given binary star system.

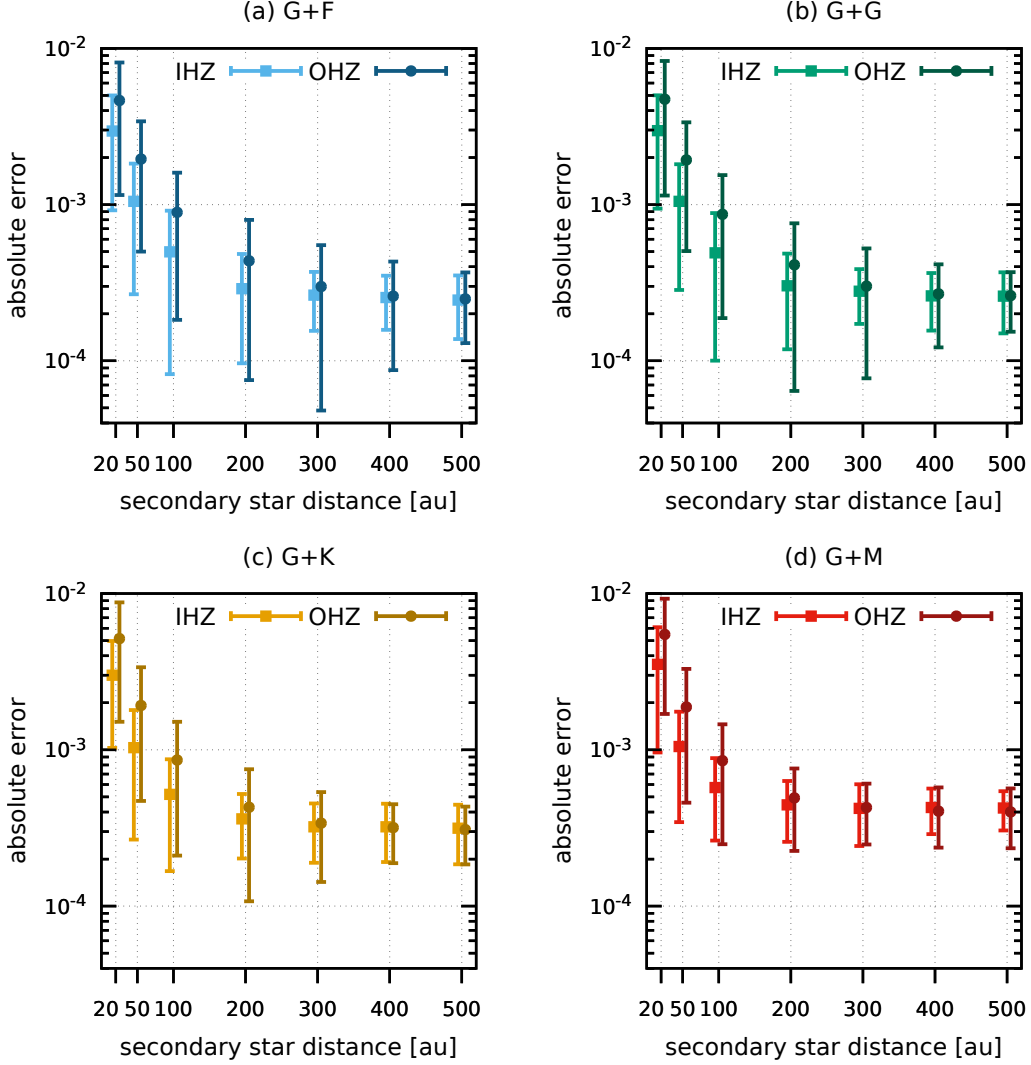


Figure 13. Comparison of absolute deviations for α_2 between the model from eq. (8) and numerical solutions based on eq. (6) (cf. tables in Appendix C). Each pair of error bars represents averaged deviations for a certain value of a_B . Symbols with squares (lighter colour) represent the deviations for the IHZ, while bullets (darker colour) mark the deviations for the OHZ. Panels (a) to (d) give details for different types of binary star systems.

These solutions of eq. (6) determine the location of the GP, a_{GP} , as a function of the secondary star’s semi-major axis, a_B , such that an SR affects some part of the HZ. The main parameters are the GP’s mass (in units of Jupiter’s mass), and the secondary star’s eccentricity e_B . The general trends of (1) decreasing α_2 with increasing a_B (i.e. the negative curvature, also visible in Fig. 2), and (2) the slight shift in α_2 with increasing e_B , like in Fig. 12, are clearly discernible from the data, too.

The numbers in the tables have been used as reference values for comparison with predictions by employing the model in eq. (8). Figure 13 shows the absolute deviations $|\Delta\alpha_2|$ between the model and the reference values from the tables. For each distance bin in a_B we computed the average error and its standard deviation ($1-\sigma$) taken over all different combinations of m_{GP} and e_B . The figure shows that for $a_B \geq 100$ au the error is less than 10^{-3} , i.e. the location of the GP that generates an SR can be determined with a typical accuracy of < 0.1 au. With smaller secondary star distance the errors are larger though, because this is a direct consequence of neglecting higher order terms in the expansion of the Laplace coefficients when deriving the simplified CAM. A closer look at the figures also reveals the trend that the errors grow steadily from G+F to G+M stars (left to right). This behaviour can be understood by the dependence of the SR region on the secondary's mass as mentioned in connection with Fig. 10: a more distant secondary must be more massive to generate the same effect as a more proximal lower-mass star. Thus, M-type companion stars are naturally closer to the GP, and so the ratio α_2 is larger, which leads to somewhat higher deviations when using eq. (8).

4. DISCUSSION

Results from earlier investigations of binary star systems assumed that well-separated binaries (beyond roughly 200 au) can be simply treated as single star systems (e.g. [Desidera and Barbieri 2007](#)). The new results presented in the previous section shed a different light on those assumptions, they demonstrate that secular perturbations do affect the HZ for a wide range of binary system orbital and physical parameters. In the following sections we will discuss some of the implications of those resonances on the dynamical evolution of test planets in the HZ.

4.1. *Effect of stellar fly-bys*

Passing stars can affect planetary systems severely and can lead to direct or indirect ejections (see review in [Davies et al. 2014](#)). A subtle effect relates to the delayed instability of planetary systems of wide binary stars induced by external perturbations, as discussed by [Kaib et al. \(2013\)](#). They explain the apparent overabundance of eccentric (circumstellar) exoplanets in wide binary systems by the

action of galactic tides that lead to an increase of the secondary star’s eccentricity. At a certain point its eccentricity is large enough for the periastron distance to drop below a critical value, below which the star triggers the instability of the exoplanetary system.

Correa-Otto and Gil-Hutton (2017) reiterate on this topic to disentangle the individual contributions of two types of external perturbations: (1) the galactic potential, and (2) stellar encounters via fly-bys. They find that stellar passages have a destabilizing effect, because 40 % of their test binary systems are disrupted, and this value is (nearly) independent of the systems’s initial eccentricity (Correa-Otto and Gil-Hutton 2017, Fig. 2). This means that a stellar fly-by, by itself, is effective in modifying the secondary’s eccentricity.

These results are verified by Bancelin et al. (2019), who study the dynamical effects of a sequence of stellar encounters between a binary star system and a passing star. Their results show that the stellar eccentricity has a maximum variance that reaches up to 0.45 for an initial stellar separation of ≥ 150 au. Hence, stellar fly-bys over an extended period of time can significantly modify the companion star’s orbital eccentricity.

Returning to Fig. 12, we can put these findings about stellar fly-bys into context with the results shown in that figure. Let us assume a binary system with an architecture such that initially the HZ is free of SR, i.e. the system would be located somewhere in the white area above one of the coloured zones. The combined effect of stellar fly-bys then can lead to a significant change (increase) of the secondary star’s eccentricity, perhaps in such a way that it enters one of the coloured bands. Consequently, an exoplanetary system with a dynamically calm HZ can transition into one that is affected by strong secular perturbations. This could turn a planet that has always had habitable conditions into a potentially uninhabitable one, depending on how much its eccentricity increases by the perturbations. The next section considers how to exactly quantify the effect of perturbations.

4.2. *Related works*

The scope of the presented model is not limited to identify and trace SR throughout the HZ of binary star systems. In an alternative embodiment of this method we could prescribe any interval of interest, not just the HZ. For instance, an application could be to check whether or not an SR

occurs at or around the location of a detected or candidate exoplanet in a multi-planet system. This can be achieved by selecting for a_{TP} an interval of distances that is different from the HZ range $a_{\text{IHZ}} \leq a_{TP} \leq a_{\text{OHZ}}$.

In the present study a major premise is that all bodies are coplanar or nearly so. As this is not generally the case, we have to consider the effect of mutual inclinations of the planets and the outer perturber. [Saleh and Rasio \(2009\)](#) have investigated the dynamics and stability of initially coplanar two-planet systems in tight binaries with an inclined stellar companion. They identified a narrow zone for the second planet that suppresses the Kozai-Lidov effect on an inner hot-Jupiter and helps to stabilize the system. [Denham et al. \(2019\)](#) improve on these former results by studying basically the same situation, but they derive an analytic stability criterion that takes into account the perturber's separation and eccentricity. Their study might be viewed as an extension of the current work to more degrees of freedom by adding an inclination to the system. They include the additional perturbations due to the Kozai-Lidov mechanism, however they only consider planetary mass perturbers in lieu of stellar masses like in our work. An extension of the current model could follow the lines of [Li and Christou \(2017\)](#) who studied SR for prograde and retrograde orbits. They constructed a semianalytical model for the restricted four-body problem that allows to describe both types of motion with a unified formalism following a suitable change of reference system. In this model resonant angles consist of linear combinations of angular differences of apsidal and nodal precession frequencies. Although the dynamical model of [Li and Christou \(2017\)](#) is similar to the one used in this paper (see section 2.2), they studied planetary satellites in very close orbits whereas we focus on rather hierarchical systems with period ratios $P_{\text{out}}/P_{\text{in}} > 2$.

Furthermore, in analogy to the current work, [Yelverton and Kennedy \(2018\)](#) have studied the influence of SR on a debris disc for the case of interior planetary perturbers. In particular, they mapped how the locations of SR depend on the masses, semi-major axes, and eccentricities of the planets.

The work of [Marzari and Gallina \(2016\)](#) also contains certain aspects from the current study. When they investigate the stability of multiplanet systems in binaries by frequency map analysis,

they identify cases when the two planets are not long-term stable although both of them are located well inside the critical stability border. They attribute this to the effect of the binary’s eccentricity and establish an empirical relationship for (a_B, e_B) to predict a critical value $a_{B,\text{crit}}$ below which the planets become unstable. For computational reasons they restricted their parameter range to $10 < a_B < 100$ au and to only three different stellar mass ratios. The CAM can be regarded as a generalization of their empirical relation that takes into account a much larger parameter space and hence covers a broader variety of use-cases. Our CAM model could also offer an explanation for the bifurcated behaviour of eccentricity excitations of exoplanets under binary perturbations that [Takeda et al. \(2008\)](#) describe in their Fig. 14. They noted that Kozai-cycles can be either suppressed or fully active in the same parameter space region for a small change in the planet’s parameters.

In [Pu and Lai \(2018\)](#) the authors focus on the same topic of a two-planet system subject to the perturbations of an external perturber. Their analysis aims to derive analytical expressions for the eccentricities of the inner planetary system as a function of the perturber’s orbital elements and mass. A main result is that a weak secular coupling between the planets (as is the case in hierarchical systems) leads to a higher susceptibility for eccentricity excitations, especially if the innermost planet is the least massive one, similar to what we have demonstrated in section [2.3.3](#).

5. SUMMARY

In this study, we investigate circumstellar planetary systems of binary stars (with coplanar and prograde motion) and the conditions that lead to secular perturbations in the habitable zone of the host star. Our main aim is to identify zones in the five-dimensional parameter space (orbital and physical parameters of the massive bodies, cf. [Fig. 1](#)) that generate dynamically unfavourable conditions for potentially habitable planets, such as elevated orbital eccentricities. This contribution helps to identify such systems in large-scale surveys and to exclude them from in-depth observations.

We apply the restricted four-body problem as dynamical model and construct a Combined Analytical Model (CAM) to systematically map the properties of different synthetic systems (see section [2.2.3](#)). Subsequently, we introduce additional simplifications to the CAM (section [2.2.4](#)) and derive explicit analytical formulas to express the resonance locations in each system parameter as a function

of the others (see Appendix B). The CAM is assessed in comparison to fully numerical results which shows that it has a median relative error less than 3 % (cf. section 3.1).

Our results are based on the properties of a sample of detected exoplanetary systems from different online databases. Secular perturbations in the HZ appear even for hierarchical wide binary systems, where stellar separations are on the order of several hundred astronomical units. We give details on the parameter combinations that generate SR in the HZ in the form of two-dimensional sections through the parameter space (section 3.2). Additionally, we derive analytical expressions to calculate the set of unfavourable giant planet positions for any given mass, semi-major axis, and eccentricity of the secondary star (in section 3.3).

Based on these results we introduce the online tool *SHaDoS* (Appendix A) that implements the CAM and provides a simple user interface to reproduce the results presented in this study.

AB and EPL are grateful for the continuous support from Austrian Science Fund (FWF) project S11608-N16, part of the National Research Network “Pathways to habitability” (PatH). We wish to thank our colleagues D. Bancelin, N. Georgakarakos, and C. Lhotka for inspiring discussion in the course of preparing this manuscript. The authors thank an anonymous reviewer whose comments and suggestions helped to improve the manuscript.

APPENDIX

A. ONLINE TOOL

We provide the online tool *SHaDoS*⁷ and allows to reproduce the results presented in this article. It implements the CAM model introduced in section 2 and solves eq. (1) for any given set of parameters. In the following we describe the main features of this tool.

The application implements an object-oriented approach with a step-by-step process for user input. There are four consecutive steps tied to the main objects of interest: (1) the host star, (2) the perturbing planet beyond the HZ, (3) the distant secondary star, and (4) the parameter space. In

⁷ This is an acronym for *Secular perturbations in Habitable zones of Double Stars*. The tool is accessible at <https://www.univie.ac.at/adg/shados/index.html>

each of these substeps the application queries for some system parameter, refer to Fig. 1 for an overview:

1. The relevant host star parameters are mass, and spectral type. Four different spectral types are preset, namely F, G, K, and M-type main-sequence stars with their respective stellar luminosity and effective temperature. Users can manually enter any other stellar characteristics, but effective temperatures are limited to the interval $2600 \leq T_{\text{eff}} \leq 7200$ K. The extent of the HZ is then computed based on this input.
2. Giant planet parameters include mass (in units of Jupiter’s mass), distance to the host star (semi-major axis), and orbital eccentricity. The eccentricity is restricted to elliptic orbits, and the distance must be larger than the outer HZ border a_{OHZ} .
3. The input for the secondary star covers its mass, distance, and eccentricity. Eccentricity is restricted to the interval $0 \leq e_B \leq 0.6$ due to limitations in the analytical model (cf. section 2.2).
4. The parameter space consists of a two-dimensional grid, where a primary parameter must be selected as the independent variable, and a secondary parameter is defined as the sought dependent variable. Available parameters are any of those depicted in Fig. 1 except for the already fixed host star mass m_A . Additionally, the minimum and maximum value of the independent variable must be entered, as well as the number of discretization steps.

After having finished all of these steps the online tool performs the calculations on-the-fly and finally displays the results. There is an option to save the resulting plot as an image in the widely supported PNG format. Any comments, suggestions, or bug reports are welcome and should be addressed to the first author.

B. SOLUTIONS FOR SIMPLIFIED CAM

Here we provide analytical solutions of the simplified CAM from eq. (7). The main goal is to express each of the parameters $(\gamma_1, \gamma_2, \alpha_1, \alpha_2, \epsilon_B)$ in turn as a function of the other four variables.

B.1. *Solutions for γ_1*

There exist two real-valued solutions for γ_1 ,

$$\gamma_{1,\pm} = \eta \left[-2\alpha_1^3 \pm (1 - \delta) \left(\eta(1 - \delta) + \sqrt{4\alpha_1^3(1 - \eta) + \eta^2(1 - \delta)^2} \right) \right] / 2\alpha_1^3, \quad (\text{B1})$$

where $\eta = \gamma_2 \alpha_2^3 \epsilon_B$, and δ is given by eq. (4). The square-root is definitely positive if $1 - \eta \geq 0$, i.e. if $\gamma_2 \alpha_2^3 \epsilon_B \leq 1$. This puts a coupled constraint on these three parameters, because it holds strictly that $0 \leq \alpha_2 < 1$, and $\epsilon_B \geq 1$, while γ_2 can be either smaller or larger than 1. Moreover, we can discard $\gamma_{1,-} < 0$ as an unphysical solution, because the mass-ratio cannot be negative. The remaining $\gamma_{1,+}$ is the preferred solution to eq. (7).

B.2. *Solution for α_1*

Apart from the trivial solution $\alpha_1 = 0$, we find

$$\alpha_1 = (1 + \gamma_1)^{1/3} \left(\frac{\eta(1 - \delta)}{\gamma_1 + \eta} \right)^{2/3}. \quad (\text{B2})$$

Note that additionally there exists also a pair of complex conjugated solutions for α_1 , but again these are not of physical interest. We caution that this functional form is only a first approximation to the ‘true’ solution of the (simplified) CAM. The formula above will give satisfactory results only if $\alpha_1 \ll 1$, i.e. typically for $\alpha_1 < 0.1$, because among all parameters α_1 is most sensitive to the assumptions made about the magnitudes of the distance ratios α_i ($i = 1, 2$). In many cases α_1 will be larger than this threshold, compare the histogram of semi-major axes in Fig. 9.

B.3. *Solutions for γ_2*

While it is straightforward to obtain the solutions for γ_1 and α_1 , there is a caveat regarding the other parameters. The problem is the explicit polynomial dependence of δ on the parameters γ_2 , α_2 , and e_B (cf. eq. (4)), which leads to rather complicated equations. One way to circumvent this issue is to linearize the equation in γ_2 by the approximation $\delta \rightarrow 0$. This is equivalent to a fall-back to the Heppenheimer formula eq. (3) and hence gives an approximation of first-order in masses. The unique linearized solution for γ_2 reads

$$\gamma_2^{(0)} = \frac{\gamma_1 \alpha_1^{3/2}}{\alpha_2^3 \epsilon_B \left((1 + \gamma_1)^{1/2} - \alpha_1^{3/2} \right)}, \quad (\text{B3})$$

where the superscript 0 denotes the approximative nature of this solution in the limit $\delta \rightarrow 0$. This solution is defined for any combination of parameters, since $(1 + \gamma_1)^{1/2} \geq 1$ and $0 \leq \alpha_1^{3/2} < 1$, so the denominator is always positive.

When considering the full equation for γ_2 we only sketch the steps to find the solutions. From [Andrade-Ines and Eggl \(2017\)](#) we observe that the correction term is $\delta(\gamma_2) \propto F(\gamma_2^{1/2}) + G(\gamma_2^{1/2}) + H(\gamma_2^2)$, where the functions F, G, H also depend on α_2 and e_B . Using the substitution $z = \gamma_2^{1/2}$ this results in a polynomial equation of degree 6 in z , for which the roots can be found with the Newton-Raphson method with initial guess $\gamma_2^{(0)}$.

B.4. Solution for α_2

On inserting the secular frequency correction term δ from eq. (4) into eq. (7) we face the problem that it would introduce fractional powers of α_2 . Hence, we restrict ourselves to the same approximation as before, $\delta \rightarrow 0$, such that no additional terms proportional to α_2 arise. The resulting equation possesses the solution

$$\alpha_2^{(0)} = \left(\frac{\gamma_1 \alpha_1^{3/2}}{\gamma_2 \epsilon_B ((1 + \gamma_1)^{1/2} - \alpha_1^{3/2})} \right)^{1/3}. \quad (\text{B4})$$

Note that it resembles eq. (B3), but the roles of γ_2 and α_2 are exchanged. A better approximation is found if we kept in δ the term $\propto \alpha_2^{3/2}$, which would give a cubic equation in $z = \alpha_2^{3/2}$.

B.5. Solutions for ϵ_B

The function δ in eq. (4) depends on the parameter e_B and involves its powers e_B^0 , e_B^2 , and e_B^4 , but eq. (7) itself contains $\epsilon_B = (1 - e_B^2)^{-3/2}$. Our goal is to achieve a simpler form of eq. (7) that should only depend on ϵ_B . In fact, the MacLaurin series expansion of ϵ_B with respect to e_B is

$$(1 - e_B^2)^{-3/2} = 1 + \frac{3}{2}e_B^2 + \frac{15}{4}e_B^4 + \mathcal{O}(e_B^6)$$

and this expansion recovers the correct powers of e_B in δ . There are other evidences that can justify the use of ϵ_B instead of e_B . First, the correction δ extends the [Heppenheimer \(1978\)](#) formula, which is a linear function of ϵ_B . Second, [Georgakarakos \(2003\)](#) and [Giuppone et al. \(2011\)](#) constructed secular models for the three-body problem that extend Heppenheimer's model to higher order in

the masses, and both new models contain some power of the expression $(1 - e_B^2)$. Following these arguments we set $\delta = \epsilon_B \left(\alpha_2^{3/2} \Gamma_1(\gamma_2) + \alpha_2^{9/2} \Gamma_2(\gamma_2) \right)$, where functions Γ_1 and Γ_2 collect all terms that depend on the parameter γ_2 . In this way δ becomes a linear function of ϵ_B . Then the full solutions are

$$\epsilon_{B,\pm} = \frac{\gamma_2 \alpha_2^3 \Delta \pm \sqrt{(\gamma_2 \alpha_2^3 \Delta)^2 - 4(1 + \gamma_1)^{1/2} \gamma_1 \gamma_2 \alpha_1^{3/2} \alpha_2^{9/2} \Gamma}}{2(1 + \gamma_1)^{1/2} \gamma_2 \alpha_2^{9/2} \Gamma}, \quad (\text{B5})$$

with the abbreviations $\Delta = (1 + \gamma_1)^{1/2} - \alpha_1^{3/2}$ ($\Delta > 0$) and $\Gamma = \Gamma_1 + \alpha_2^3 \Gamma_2$. Note that $\epsilon_B \geq 1$ in order to be a physically relevant solution.

C. TABLES

Table 3. G+F binary stars for different giant planet masses.

a_B [AU]	$m_{GP} = 1 M_J$		$m_{GP} = 3 M_J$		$m_{GP} = 5 M_J$	
	$\alpha_{2,IHZ}$	$\alpha_{2,OHZ}$	$\alpha_{2,IHZ}$	$\alpha_{2,OHZ}$	$\alpha_{2,IHZ}$	$\alpha_{2,OHZ}$
$e_B = 0.0$						
20	0.088	0.120	0.103	0.135	0.112	0.144
50	0.058	0.074	0.071	0.088	0.078	0.096
100	0.044	0.055	0.055	0.067	0.061	0.074
200	0.034	0.042	0.043	0.053	0.048	0.058
300	0.030	0.036	0.038	0.046	0.042	0.051
400	0.027	0.033	0.034	0.042	0.038	0.046
500	0.025	0.031	0.032	0.039	0.036	0.043
$e_B = 0.2$						
20	0.087	0.119	0.102	0.134	0.110	0.141
50	0.057	0.073	0.070	0.087	0.077	0.095
100	0.044	0.054	0.054	0.067	0.060	0.074
200	0.034	0.042	0.043	0.052	0.048	0.058
300	0.030	0.036	0.037	0.045	0.042	0.050
400	0.027	0.033	0.034	0.041	0.038	0.046
500	0.025	0.030	0.032	0.038	0.035	0.042
$e_B = 0.4$						
20	0.083	0.114	0.100	0.126	0.104	0.132
50	0.055	0.070	0.067	0.083	0.073	0.090
100	0.042	0.052	0.052	0.064	0.058	0.070
200	0.033	0.040	0.041	0.050	0.046	0.055
300	0.028	0.034	0.036	0.043	0.040	0.048
400	0.026	0.031	0.032	0.039	0.036	0.044
500	0.024	0.029	0.030	0.036	0.034	0.041
$e_B = 0.6$						
20	0.076	0.104	0.100	0.113	0.100	0.118
50	0.050	0.064	0.060	0.074	0.065	0.080
100	0.038	0.047	0.047	0.057	0.052	0.062
200	0.029	0.036	0.037	0.045	0.041	0.049
300	0.026	0.031	0.032	0.039	0.036	0.043
400	0.023	0.028	0.029	0.035	0.033	0.039
500	0.022	0.026	0.027	0.033	0.030	0.037

Table 4. G+G binary stars for different giant planet masses

a_B [AU]	$m_{GP} = 1 M_J$		$m_{GP} = 3 M_J$		$m_{GP} = 5 M_J$	
	$\alpha_{2,IHZ}$	$\alpha_{2,OHZ}$	$\alpha_{2,IHZ}$	$\alpha_{2,OHZ}$	$\alpha_{2,IHZ}$	$\alpha_{2,OHZ}$
$e_B = 0.0$						
20	0.092	0.125	0.108	0.141	0.118	0.150
50	0.061	0.077	0.075	0.093	0.082	0.102
100	0.047	0.058	0.058	0.071	0.065	0.079
200	0.036	0.044	0.046	0.056	0.051	0.062
300	0.032	0.039	0.040	0.049	0.045	0.054
400	0.029	0.035	0.036	0.044	0.041	0.049
500	0.027	0.032	0.034	0.041	0.038	0.046
$e_B = 0.2$						
20	0.091	0.124	0.107	0.139	0.116	0.148
50	0.060	0.077	0.074	0.092	0.081	0.101
100	0.046	0.057	0.058	0.070	0.064	0.078
200	0.036	0.044	0.045	0.055	0.051	0.061
300	0.031	0.038	0.040	0.048	0.044	0.053
400	0.028	0.034	0.036	0.044	0.040	0.049
500	0.026	0.032	0.033	0.040	0.037	0.045
$e_B = 0.4$						
20	0.087	0.118	0.102	0.131	0.110	0.139
50	0.058	0.074	0.070	0.088	0.077	0.095
100	0.044	0.055	0.055	0.067	0.061	0.074
200	0.034	0.042	0.043	0.053	0.048	0.058
300	0.030	0.036	0.038	0.046	0.042	0.051
400	0.027	0.033	0.034	0.042	0.038	0.046
500	0.025	0.030	0.032	0.039	0.036	0.043
$e_B = 0.6$						
20	0.079	0.108	0.100	0.118	0.100	0.123
50	0.052	0.067	0.063	0.078	0.069	0.085
100	0.040	0.050	0.050	0.060	0.055	0.066
200	0.031	0.038	0.039	0.047	0.044	0.052
300	0.027	0.033	0.034	0.041	0.038	0.046
400	0.025	0.030	0.031	0.038	0.035	0.042
500	0.023	0.028	0.029	0.035	0.032	0.039

Table 5. G+K binary stars for different giant planet masses

a_B [AU]	$m_{GP} = 1 M_J$		$m_{GP} = 3 M_J$		$m_{GP} = 5 M_J$	
	$\alpha_{2,IHZ}$	$\alpha_{2,OHZ}$	$\alpha_{2,IHZ}$	$\alpha_{2,OHZ}$	$\alpha_{2,IHZ}$	$\alpha_{2,OHZ}$
$e_B = 0.0$						
20	0.098	0.132	0.116	0.150	0.126	0.161
50	0.065	0.083	0.081	0.100	0.089	0.110
100	0.050	0.062	0.063	0.077	0.070	0.085
200	0.039	0.048	0.050	0.060	0.056	0.067
300	0.034	0.042	0.043	0.053	0.049	0.059
400	0.031	0.038	0.039	0.048	0.044	0.053
500	0.029	0.035	0.037	0.044	0.041	0.049
$e_B = 0.2$						
20	0.097	0.130	0.115	0.148	0.125	0.158
50	0.065	0.082	0.080	0.099	0.088	0.108
100	0.050	0.061	0.062	0.076	0.069	0.084
200	0.039	0.047	0.049	0.060	0.055	0.066
300	0.034	0.041	0.043	0.052	0.048	0.058
400	0.031	0.037	0.039	0.047	0.044	0.053
500	0.028	0.035	0.036	0.044	0.040	0.049
$e_B = 0.4$						
20	0.093	0.124	0.109	0.140	0.118	0.148
50	0.062	0.079	0.076	0.094	0.084	0.103
100	0.048	0.059	0.060	0.073	0.066	0.080
200	0.037	0.045	0.047	0.057	0.052	0.063
300	0.032	0.039	0.041	0.050	0.046	0.055
400	0.029	0.036	0.037	0.045	0.042	0.050
500	0.027	0.033	0.035	0.042	0.039	0.047
$e_B = 0.6$						
20	0.084	0.113	0.100	0.125	0.105	0.131
50	0.056	0.071	0.068	0.084	0.075	0.091
100	0.043	0.053	0.054	0.065	0.059	0.072
200	0.034	0.041	0.043	0.051	0.047	0.057
300	0.029	0.036	0.037	0.045	0.041	0.050
400	0.027	0.032	0.034	0.041	0.038	0.045
500	0.025	0.030	0.031	0.038	0.035	0.042

Table 6. G+M binary stars for different giant planet masses

a_B [AU]	$m_{GP} = 1 M_J$		$m_{GP} = 3 M_J$		$m_{GP} = 5 M_J$	
	$\alpha_{2,IHZ}$	$\alpha_{2,OHZ}$	$\alpha_{2,IHZ}$	$\alpha_{2,OHZ}$	$\alpha_{2,IHZ}$	$\alpha_{2,OHZ}$
$e_B = 0.0$						
20	0.108	0.144	0.130	0.166	0.142	0.179
50	0.073	0.092	0.091	0.112	0.101	0.124
100	0.057	0.070	0.071	0.087	0.079	0.097
200	0.045	0.054	0.056	0.068	0.063	0.076
300	0.039	0.047	0.049	0.060	0.055	0.066
400	0.035	0.043	0.045	0.054	0.050	0.060
500	0.033	0.040	0.042	0.050	0.046	0.056
$e_B = 0.2$						
20	0.107	0.142	0.128	0.164	0.140	0.176
50	0.072	0.091	0.090	0.111	0.100	0.122
100	0.056	0.069	0.071	0.086	0.078	0.095
200	0.044	0.054	0.056	0.067	0.062	0.075
300	0.038	0.047	0.049	0.059	0.054	0.066
400	0.035	0.042	0.044	0.053	0.049	0.060
500	0.032	0.039	0.041	0.050	0.046	0.055
$e_B = 0.4$						
20	0.103	0.136	0.122	0.154	0.132	0.165
50	0.069	0.087	0.086	0.106	0.095	0.116
100	0.054	0.066	0.067	0.082	0.075	0.091
200	0.042	0.051	0.053	0.064	0.059	0.072
300	0.037	0.044	0.046	0.056	0.052	0.063
400	0.033	0.040	0.042	0.051	0.047	0.057
500	0.031	0.037	0.039	0.047	0.044	0.053
$e_B = 0.6$						
20	0.093	0.124	0.109	0.138	0.118	0.146
50	0.063	0.080	0.077	0.095	0.085	0.103
100	0.049	0.060	0.061	0.074	0.068	0.082
200	0.038	0.047	0.048	0.058	0.054	0.065
300	0.033	0.040	0.042	0.051	0.047	0.057
400	0.030	0.037	0.038	0.046	0.043	0.052
500	0.028	0.034	0.036	0.043	0.040	0.048

REFERENCES

- Andrade-Ines, E. and Eggl, S. (2017). Secular Orbit Evolution in Systems with a Strong External Perturber - A Simple and Accurate Model. *AJ*, 153:148.
- Bancelin, D., Nordlander, T., Pilat-Lohinger, E., and Loibnegger, B. (2019). Dynamics of passing-stars-perturbed binary star systems. *MNRAS*, 486(4):4773–4780.
- Bancelin, D., Pilat-Lohinger, E., and Bazsó, Á. (2016). Asteroid flux towards circumprimary habitable zones in binary star systems. II. Dynamics. *A&A*, 591:A120.
- Bazsó, Á. and Pilat-Lohinger, E. (2017). Analytical estimates of secular frequencies for binary star systems. *Proceedings of the First Greek-Austrian Workshop on Extrasolar Planetary Systems*, pages 45–61.
- Bazsó, Á., Pilat-Lohinger, E., Eggl, S., Funk, B., Bancelin, D., and Rau, G. (2017). Dynamics and habitability in circumstellar planetary systems of known binary stars. *MNRAS*, 466:1555–1566.
- Boss, A. P. (2006). Gas Giant Protoplanets Formed by Disk Instability in Binary Star Systems. *ApJ*, 641:1148–1161.
- Bromley, B. C. and Kenyon, S. J. (2015). Planet Formation around Binary Stars: Tatooine Made Easy. *ApJ*, 806:98.
- Bryan, M. L., Knutson, H. A., Howard, A. W., Ngo, H., Batygin, K., Crepp, J. R., Fulton, B. J., Hinkley, S., Isaacson, H., Johnson, J. A., Marcy, G. W., and Wright, J. T. (2016). Statistics of Long Period Gas Giant Planets in Known Planetary Systems. *ApJ*, 821(2):89.
- Chambers, J. E. (1999). A hybrid symplectic integrator that permits close encounters between massive bodies. *MNRAS*, 304:793–799.
- Christou, A. A. and Murray, C. D. (1999). The effect of near resonances on the secular precession of close orbits. *MNRAS*, 303(4):806–812.
- Correa-Otto, J. A. and Gil-Hutton, R. A. (2017). Galactic perturbations on the population of wide binary stars with exoplanets. *A&A*, 608:A116.
- Cumming, A., Butler, R. P., Marcy, G. W., Vogt, S. S., Wright, J. T., and Fischer, D. A. (2008). The Keck Planet Search: Detectability and the Minimum Mass and Orbital Period Distribution of Extrasolar Planets. *PASP*, 120(867):531.
- Cuntz, M. (2014). S-type and P-type Habitability in Stellar Binary Systems: A Comprehensive Approach. I. Method and Applications. *ApJ*, 780:14.

- Davies, M. B., Adams, F. C., Armitage, P., Chambers, J., Ford, E., Morbidelli, A., Raymond, S. N., and Veras, D. (2014). The Long-Term Dynamical Evolution of Planetary Systems. In Beuther, H., Klessen, R. S., Dullemond, C. P., and Henning, T., editors, *Protostars and Planets VI*, page 787.
- Denham, P., Naoz, S., Hoang, B.-M., Stephan, A. P., and Farr, W. M. (2019). Hidden planetary friends: on the stability of two-planet systems in the presence of a distant, inclined companion. *MNRAS*, 482(3):4146–4154.
- Desidera, S. and Barbieri, M. (2007). Properties of planets in binary systems. The role of binary separation. *A&A*, 462:345–353.
- Duchêne, G. and Kraus, A. (2013). Stellar Multiplicity. *ARA&A*, 51:269–310.
- Duquennoy, A., Mayor, M., and Halbwachs, J.-L. (1991). Multiplicity among solar type stars in the solar neighbourhood. I - CORAVEL radial velocity observations of 291 stars. *A&AS*, 88:281–324.
- Dvorak, R. (1982). Planetenbahnen in Doppelsternsystemen. *Oesterreichische Akademie Wissenschaften Mathematisch naturwissenschaftliche Klasse Sitzungsberichte Abteilung*, 191(10):423–437.
- Eggl, S., Pilat-Lohinger, E., Georgakarakos, N., Gyergyovits, M., and Funk, B. (2012). An Analytic Method to Determine Habitable Zones for S-Type Planetary Orbits in Binary Star Systems. *ApJ*, 752:74.
- Frouard, J., Fouchard, M., and Vienne, A. (2010). About the dynamics of the evection resonance. *A&A*, 515:A54.
- Funk, B., Pilat-Lohinger, E., and Eggl, S. (2015). Can there be additional rocky planets in the Habitable Zone of tight binary stars with a known gas giant? *MNRAS*, 448:3797–3805.
- Gayon, J. and Bois, E. (2008). Are retrograde resonances possible in multi-planet systems? *A&A*, 482(2):665–672.
- Georgakarakos, N. (2003). Eccentricity evolution in hierarchical triple systems with eccentric outer binaries. *MNRAS*, 345:340–348.
- Georgakarakos, N. (2009). Improved equations for eccentricity generation in hierarchical triple systems. *MNRAS*, 392:1253–1263.
- Giuppone, C. A., Leiva, A. M., Correa-Otto, J., and Beaugé, C. (2011). Secular dynamics of planetesimals in tight binary systems: application to γ -Cephei. *A&A*, 530:A103.
- Hadden, S. and Lithwick, Y. (2018). A Criterion for the Onset of Chaos in Systems of Two Eccentric Planets. *AJ*, 156(3):95.
- Heppenheimer, T. A. (1978). On the formation of planets in binary star systems. *A&A*, 65:421–426.
- Holman, M. J. and Wiegert, P. A. (1999). Long-Term Stability of Planets in Binary Systems. *AJ*, 117:621–628.
- Jang-Condell, H. (2015). On the Likelihood of Planet Formation in Close Binaries. *ApJ*, 799:147.

- Kaib, N. A., Raymond, S. N., and Duncan, M. (2013). Planetary system disruption by Galactic perturbations to wide binary stars. *Nature*, 493:381–384.
- Kaltenegger, L. and Haghighipour, N. (2013). Calculating the Habitable Zone of Binary Star Systems. I. S-type Binaries. *ApJ*, 777:165.
- Kasting, J. F., Whitmire, D. P., and Reynolds, R. T. (1993). Habitable Zones around Main Sequence Stars. *Icarus*, 101:108–128.
- Kley, W. and Nelson, R. P. (2010). Early Evolution of Planets in Binaries: Planet-Disk Interaction. In Haghighipour, N., editor, *Planets in Binary Star Systems*, volume 366 of *Astrophysics and Space Science Library*, page 135.
- Knezevic, Z., Milani, A., Farinella, P., Froeschle, C., and Froeschle, C. (1991). Secular resonances from 2 to 50 AU. *Icarus*, 93:316–330.
- Kopparapu, R. K., Ramirez, R. M., SchottelKotte, J., Kasting, J. F., Domagal-Goldman, S., and Eymet, V. (2014). Habitable Zones around Main-sequence Stars: Dependence on Planetary Mass. *ApJL*, 787:L29.
- Kraus, A. L., Ireland, M. J., Huber, D., Mann, A. W., and Dupuy, T. J. (2016). The Impact of Stellar Multiplicity on Planetary Systems. I. The Ruinous Influence of Close Binary Companions. *AJ*, 152(1):8.
- Laskar, J. (1999). Introduction to frequency map analysis. In Simo, C., editor, *NATO ASI Hamiltonian Systems with Three or More Degrees of Freedom*, pages 134–150. Kluwer, Dordrecht.
- Li, D. and Christou, A. A. (2017). Secular resonances between bodies on close orbits II: prograde and retrograde orbits for irregular satellites. *Celestial Mechanics and Dynamical Astronomy*, 129(1-2):1–23.
- Malhotra, R. (1998). Orbital Resonances and Chaos in the Solar System. In Lazzaro, D., Vieira Martins, R., Ferraz-Mello, S., and Fernandez, J., editors, *Solar System Formation and Evolution*, volume 149 of *Astronomical Society of the Pacific Conference Series*, page 37.
- Marzari, F. and Gallina, G. (2016). Stability of multiplanet systems in binaries. *A&A*, 594:A89.
- Milani, A. and Knezevic, Z. (1990). Secular perturbation theory and computation of asteroid proper elements. *Celestial Mechanics and Dynamical Astronomy*, 49(4):347–411.
- Morais, M. H. M. and Giuppone, C. A. (2012). Stability of prograde and retrograde planets in circular binary systems. *MNRAS*, 424(1):52–64.
- Morais, M. H. M. and Namouni, F. (2013). Retrograde resonance in the planar three-body problem. *Celestial Mechanics and Dynamical Astronomy*, 117(4):405–421.

- Mudryk, L. R. and Wu, Y. (2006). Resonance Overlap Is Responsible for Ejecting Planets in Binary Systems. *ApJ*, 639:423–431.
- Mugrauer, M. and Neuhäuser, R. (2009). The multiplicity of exoplanet host stars. New low-mass stellar companions of the exoplanet host stars HD 125612 and HD 212301. *A&A*, 494:373–378.
- Müller, T. W. A. and Kley, W. (2012). Circumstellar disks in binary star systems. Models for γ Cephei and α Centauri. *A&A*, 539:A18.
- Murray, C. D. and Dermott, S. F. (1999). *Solar system dynamics*. Cambridge University Press.
- Naoz, S., Farr, W. M., Lithwick, Y., Rasio, F. A., and Teyssandier, J. (2013). Secular dynamics in hierarchical three-body systems. *MNRAS*, 431(3):2155–2171.
- Perryman, M. (2011). *The Exoplanet Handbook*. Cambridge University Press.
- Pilat-Lohinger, E. (2005). Planetary motion in double stars: the influence of the secondary. In Knežević, Z. and Milani, A., editors, *IAU Colloq. 197: Dynamics of Populations of Planetary Systems*, pages 71–76.
- Pilat-Lohinger, E., Bazsó, Á., and Funk, B. (2016). A Quick Method to Identify Secular Resonances in Multi-planet Systems with a Binary Companion. *AJ*, 152:139.
- Pilat-Lohinger, E. and Dvorak, R. (2002). Stability of S-type Orbits in Binaries. *CMDA*, 82:143–153.
- Pilat-Lohinger, E., Sándor, Z., Gyergyovits, M., and Bazsó, Á. (2019). Planets in Binary Stars. In *Accretion Processes in Cosmic Sources II (APCS2018). Accretion Onto Planets*, volume 342.
- Pu, B. and Lai, D. (2018). Eccentricities and inclinations of multiplanet systems with external perturbers. *MNRAS*, 478(1):197–217.
- Quintana, E. V., Adams, F. C., Lissauer, J. J., and Chambers, J. E. (2007). Terrestrial Planet Formation around Individual Stars within Binary Star Systems. *ApJ*, 660:807–822.
- Rabl, G. and Dvorak, R. (1988). Satellite-type planetary orbits in double stars : a numerical approach. *A&A*, 191:385–391.
- Rafikov, R. R. (2013). Planet Formation in Small Separation Binaries: Not so Secularly Excited by the Companion. *ApJL*, 765(1):L8.
- Raghavan, D., Henry, T. J., Mason, B. D., Subasavage, J. P., Jao, W.-C., Beaulieu, T. D., and Hambly, N. C. (2006). Two Suns in The Sky: Stellar Multiplicity in Exoplanet Systems. *ApJ*, 646:523–542.
- Raghavan, D., McAlister, H. A., Henry, T. J., Latham, D. W., Marcy, G. W., Mason, B. D., Gies, D. R., White, R. J., and ten Brummelaar, T. A. (2010). A Survey of Stellar Families: Multiplicity of Solar-type Stars. *ApJS*, 190:1–42.

- Robutel, P. and Laskar, J. (2001). Frequency Map and Global Dynamics in the Solar System I. Short Period Dynamics of Massless Particles. *Icarus*, 152:4–28.
- Roell, T., Neuhäuser, R., Seifahrt, A., and Mugrauer, M. (2012). Extrasolar planets in stellar multiple systems. *A&A*, 542:A92.
- Saleh, L. A. and Rasio, F. A. (2009). The Stability and Dynamics of Planets in Tight Binary Systems. *ApJ*, 694(2):1566–1576.
- Schneider, J., Dedieu, C., Le Sidaner, P., Savalle, R., and Zolotukhin, I. (2011). Defining and cataloging exoplanets: the exoplanet.eu database. *A&A*, 532:A79.
- Schwarz, R., Funk, B., Zechner, R., and Bazzó, Á. (2016). New prospects for observing and cataloging exoplanets in well-detached binaries. *MNRAS*, 460:3598–3609.
- Takeda, G., Kita, R., and Rasio, F. A. (2008). Planetary Systems in Binaries. I. Dynamical Classification. *ApJ*, 683(2):1063–1075.
- Thebault, P. and Haghighipour, N. (2015). Planet Formation in Binaries. In Jin, S., Haghighipour, N., and Ip, W.-H., editors, *Planetary Exploration and Science: Recent Results and Advances*, Springer Geophysics, Springer-Verlag, Berlin Heidelberg, pages 309–340.
- Tokovinin, A. (2014). From Binaries to Multiples. II. Hierarchical Multiplicity of F and G Dwarfs. *AJ*, 147:87.
- Touma, J. R. and Sridhar, S. (2015). The disruption of multiplanet systems through resonance with a binary orbit. *Nature*, 524(7566):439–441.
- Šidlichovský, M. and Nesvorný, D. (1996). Frequency modified Fourier transform and its applications to asteroids. *Celestial Mechanics and Dynamical Astronomy*, 65(1-2):137–148.
- Wang, J., Fischer, D. A., Xie, J.-W., and Ciardi, D. R. (2014). Influence of Stellar Multiplicity on Planet Formation. II. Planets are Less Common in Multiple-star Systems with Separations Smaller than 1500 AU. *ApJ*, 791:111.
- Wang, Z. and Cuntz, M. (2019). S-type and P-type Habitability in Stellar Binary Systems: A Comprehensive Approach. III. Results for Mars, Earth, and Super-Earth Planets. *ApJ*, 873:113.
- Yelverton, B. and Kennedy, G. M. (2018). Empty gaps? Depleting annular regions in debris discs by secular resonance with a two-planet system. *MNRAS*, 479(2):2673–2691.
- Zhou, J.-L., Xie, J.-W., Liu, H.-G., Zhang, H., and Sun, Y.-S. (2012). Forming different planetary systems. *Research in Astronomy and Astrophysics*, 12(8):1081–1106.